Chemical Engineering Journal 519 (2025) 163598

Contents lists available at ScienceDirect

Chemical Engineering Journal

journal homepage: www.elsevier.com/locate/cej

Enabling micro-kinetics based simulation of industrial packed-bed reactors by physics-enhanced neural networks☆

Felix Biermann [a], Riccardo Uglietti [b,*], Felix A. Döppel [a], Tim Kircher [a], Mauro Bracconi [c,*], Matteo Maestri [c,*], Martin Votsmeier [a,b,*]

[a] Technische Universität Darmstadt, Peter-Grünberg-Straße 8, 64287 Darmstadt, Germany
[b] Umicore AG & Co. KG, Rodenbacher Chaussee 4, 63457 Hanau, Germany
[c] Politecnico di Milano 20156 Milano, Italy

ARTICLE INFO

Keywords:
Machine learning
Neural networks
Multiscale modeling
Kinetic modeling
Micro-kinetics
Industrial Modeling

ABSTRACT

Multiscale CFD simulations can provide insights into the coupling of the surface catalytic mechanism and reactor scale transport phenomena. To address the high computational cost of detailed micro-kinetic models, we have applied for the first time artificial neural networks (NNs) as surrogate models for micro-kinetic rate evaluations, with the aim of accelerating particle-resolved CFD simulations of a catalytic reactor. To evaluate the efficacy of the proposed strategy, a methane steam reforming packed bed reactor was selected as a benchmark case. A global reaction neural network with embedded thermodynamic and stoichiometric information has been implemented as a surrogate for a UBI-QEP micro-kinetic model available in literature. Two distinct test cases have been employed. The first targets a lab scale reactor, enabling either the full evaluation of the micro-kinetic scheme or the novel NN accelerated approach in the CFD simulations. The comparison between the two strategies showed deviations in the computed mole fractions of less than 1 % across a wide range of operating conditions along with a 19-fold total simulation and 63-fold chemistry speed-up. Consequently, the total simulation time of the benchmark was reduced from 114 h to 6 h, with only 29.2 % or 1.75 h of the computational cost being allocated to the chemistry sub-step of the solver. Therefore, source term evaluations are no longer the bottleneck of reactive CFD. Given the obtained excellent accuracy and speed-up, we applied the NN-accelerated micro-kinetics to the CFD simulation of an industrial scale packed-bed reactor, discretized with 44 M cells (54 % solid phase). To the best of our knowledge, this represents the largest reactive simulation with micro-kinetic level of detail. Overall, these results pave the way for the scale-up of multiscale simulations to industrially relevant scales.

1. Introduction

Heterogeneous catalysis plays a central role in the current transformation of the chemical industry, e.g. for the chemical valorization of CO_2. Both the investigation of novel processes, and the optimization of existing reactor designs, require an increasingly detailed comprehension of the catalytic system [1–4]. In particular, it is not only sufficient to understand the reactive mechanism acting on the catalyst, but it is equally important to predict how the chemistry is affected by transport phenomena.

To achieve this level of comprehension, it is essential to be able to investigate the coupled physical and chemical mechanisms in the actual geometry of interest. In this context, multiscale numerical simulations have gained more and more importance [1,4–6]. However, this approach requires the coupling between the detailed modeling of fluid dynamics through the catalytic bed, the intraparticle diffusion within the catalytically active pellets of the bed and the catalyst kinetics. The fluid flow is usually described by means of Computational Fluid Dynamics (CFD). The detailed description of the chemical reactions evolving on the catalytic sites of the pellets is typically the origin of most of the computational cost. In particular, the computational effort depends on the complexity of the reaction network and the required detail in the kinetic model. Micro-kinetic models are usually stiff systems of ordinary differential (ODE) equations that require a high percentage of

☆ This article is part of a special issue entitled: 'ISCRE 28' published in Chemical Engineering Journal.

* Corresponding authors.
E-mail addresses: riccardo.uglietti@eu.umicore.com (R. Uglietti), mauro.bracconi@polimi.it (M. Bracconi), matteo.maestri@polimi.it (M. Maestri), martin.votsmeier@tu-darmstadt.de (M. Votsmeier).

https://doi.org/10.1016/j.cej.2025.163598

Available online 19 May 2025

the overall computational resources [7,8] in catalytic CFD simulations. Moreover, more detailed kinetic modeling techniques, e.g. kinetic Monte Carlo, cannot be directly included in CFD but require specific methodologies to achieve an effective coupling [7,9]. Hence, an extensive effort is ongoing in the last years to properly manage the inevitable complexity of the catalytic models, enabling their application in CFD simulations of relevant reactor geometries and operating conditions [7].

Two primary approaches have been employed in the treatment of catalytic kinetics: in-situ (during runtime) and ex-situ (before runtime). In-situ approaches include in-situ adaptive tabulation [1,8,10–12] and cell agglomeration [1,13] occasionally applied even at the same time [12,14]. They reduce the number of integrations of the kinetic model, but their optimal setting is system dependent, hampering the effortless application of these speed-up techniques to arbitrarily complex systems. Ex-situ approaches consisted initially in the simplification/reduction of the catalytic mechanism, which is performed mainly through time scale analysis [15–20] or error based strategies [21–23]. A commonly employed strategy is deriving a global reaction mechanism from a detailed micro-kinetic mechanism [24–26]. This approach requires a specific analysis for each investigated mechanism, and presents a system dependent accuracy [27]. Furthermore, the derivation of global reaction models relies on assuming a rate determining step, and for the same mechanism different rate determining steps can be observed as a function of operating conditions. Therefore, the ex-situ approach has evolved towards replacing the catalytic kinetics with surrogated models, which predict effective source terms under steady state surface coverages. This approach is generally justified, because surface species are immobile on the reactor length scale [28,29]. Initially, multi-variate spline interpolation was used for predicting the source terms [28,30–32]. This approach was extended to predict the solution of the lower scale reaction–diffusion problem [33], or even the solution of a complete volume element [34]. Despite a good accuracy, splines proved to be unsuitable for surrogate models with more than about 6 relevant input dimensions [35]. The application range of the spline surrogates could be extended to about 8 dimensions by the introduction of Hermite splines [35].

Consequently, in the last years, machine learning (ML) algorithms have gained increasing attention to effectively and efficiently bridge the scales in multiscale simulations, as discussed in reviews by Bruix *et al.* [5] and Bracconi [36] and considered as one of the "urgent" research needs of chemical reaction engineering. Indeed, ML techniques are significantly less affected by the curse of dimensionality and are thus applicable for more complex reactive systems. For instance, Döppel & Votsmeier [37] showed that artificial neural networks (NNs) outperform spline interpolation by orders of magnitude with respect to the prediction time and the storage space [37]. Additionally, ML algorithms allow for the development of adaptive sampling techniques, which reduces the amount of required training data [7,38].

Initially, the potential of random forests [7,39] for catalytic rate predictions was examined, and they were subsequently integrated into a catalytic CFD simulation. The first successful implementation was reported by Partopour *et al.* [39]. They employed a surrogate model to describe catalytic ethylene oxidation in a fixed-bed reactor and demonstrated that the random forests are capable of outperforming multivariate spline interpolation. Moreover, Bracconi & Maestri [7] applied random forests to predict steady-state coverages of a first-principle kinetic Monte Carlo model for CO oxidation on $RuO_2(110)$ [40]. Further interpolation and machine learning algorithms applied as surrogate models are kernel methods [38] and sparse grids [41].

Recently, an increasing number of works have been published, focusing on the application of NNs to the prediction of surface reaction rates [37,42–46]. In contrast to random forests, the average time for a single rate-prediction in NN only correlates weakly with its number of parameters [43]. Indeed, the number of nodes and layers, constituting the NN, can be increased without significant impact on the prediction time, which is a crucial parameter due to the millions of cells typically present in a simulation. Additionally, analytical derivatives of NNs are easily computed, e.g., contributing to a fast linearization of the chemical source term in steady-state catalytic simulations.

One further advantage of NNs is due to the utilization of back-propagation during training and the availability of efficient automatic differentiation frameworks, physical constraints can be easily implemented in the network architecture, greatly improving their accuracy and data efficiency. For example, atom conservation can be implemented in the NN, so that the learned solutions are stoichiometrically consistent by design [47–51]. Recently, also thermodynamic constraints have been implemented [45,46,52]. In this work we apply our recently developed Global Reaction Neural Networks (GRNN) [46,53,54], which embed a priori thermodynamic and stoichiometric information. By embedding physical information, the computational cost is reduced, and the extrapolation behavior of the surrogate model is improved, significantly reducing at the same time the amount of training data. Despite the advantages discussed along with their accuracy in chemical source term predictions, a catalytic CFD model accelerated by NNs is still not available.

In this work, we enable the efficient coupling of fluid dynamics reactor models with arbitrarily complex detailed micro-kinetic models via the adoption of NN surrogates in CFD simulations. To achieve this goal, we extend the catalyticFOAM framework [55], targeted to the CFD simulation of 3D catalytic domains, with a new interface, enabling the integration of surrogate neural network kinetic models with arbitrary network architectures. The new interface is demonstrated by implementing our previously developed GRNN. Methane steam reforming (MSR) is used as a benchmark to assess the performance of the so obtained NN-enhanced framework. In particular, the surface chemistry was described by a UBI-QEP [56] based surface kinetic model proposed by Maestri *et al.* [14]. In the following we demonstrate our approach by implementing two models for a lab scale (2.54 cm in diameter) as well as an industrial scale (10.28 cm in diameter) cylindrical packed bed tube reactor.

The lab scale reactor was simulated by means of both micro-kinetic and NN-accelerated CFD approaches to directly compare the two approaches. To assess the applicability of the GRNN model, the inlet velocity was varied to cover a wide conversion range. The relative error was obtained for all the NN-accelerated simulations with respect to their reference micro-kinetic ones. Furthermore, an average speed-up of the chemistry sub-step and a total simulation speed-up was evaluated.

Finally, to demonstrate the potential of the proposed approach, the GRNN-accelerated solver has been applied to a packed bed reactor with industrially relevant diameter. To the best knowledge of the authors, this represents the largest particle-resolved CFD model with full micro-kinetic details that has been published to date. In the context of catalytically active computational cells, its size is comparable to the overall largest particle-resolved CFD case, which was published by Kutscherauer [24,26] and simulated with global kinetics.

The proposed methodology is applicable to any heterogeneous system and is not limited to packed bed reactors or methane steam reforming. We therefore believe that this work facilitates the transition from particle-resolved CFD simulations to the industrial scale while preserving the chemical information, thanks to the drastic reduction of the computational cost associated with the detailed chemistry via physics enhanced neural networks. The proposed methodology paves the way for an increased application of particle-resolved CFD micro-kinetic models to relevant scales, enabling a better reactor design and optimization.

2. Methods

This section first introduces the solver that has been employed for the catalytic CFD simulations of the packed bed reactors considered in this work. Subsequently, the focus shifts to the discussion of the CFD solver accelerated by neural networks (NNs). Then, the Global Reaction Neural Network (GRNN) surrogate model used in this work and metrics to

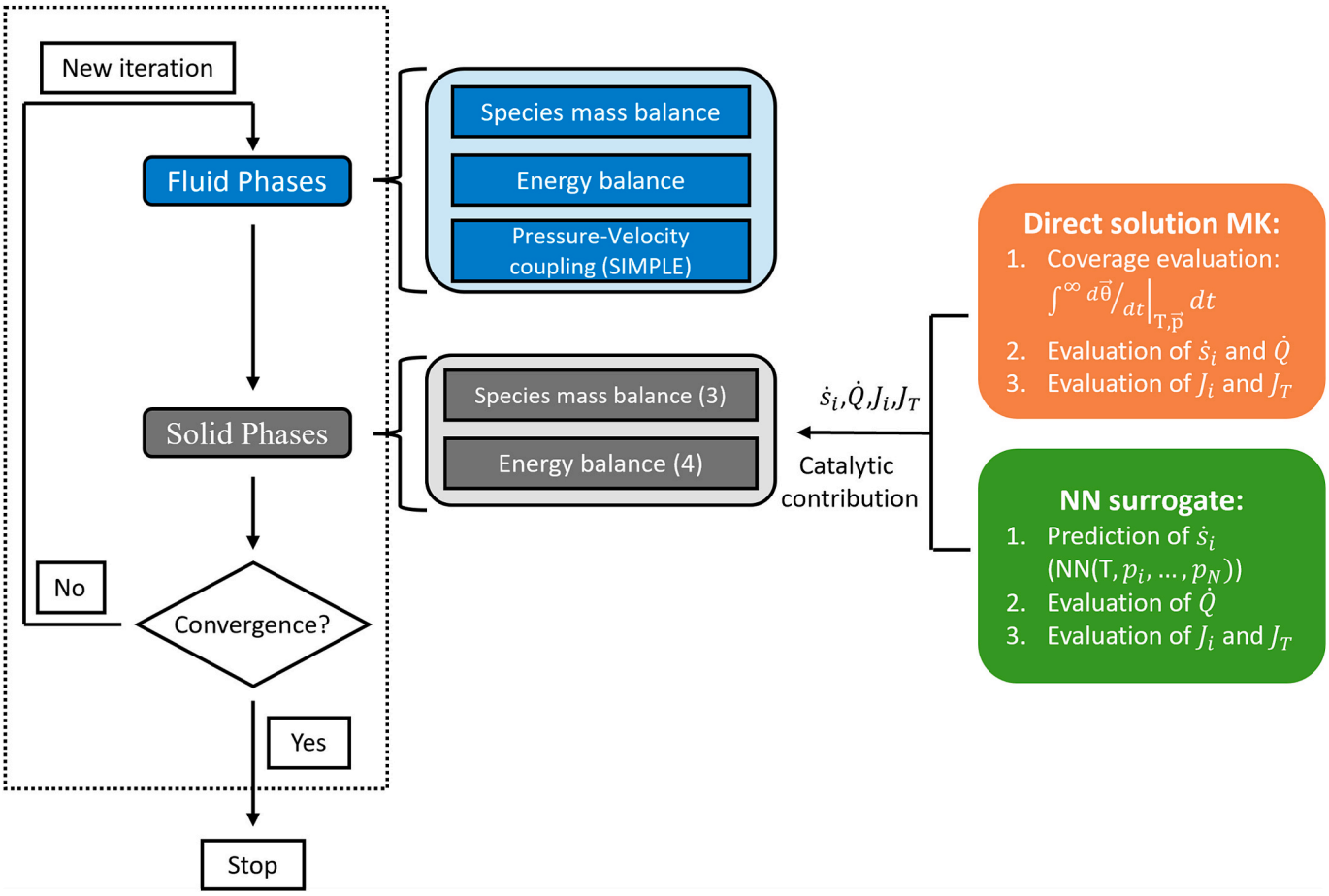

Fig. 1. Simplified flowchart of the solution algorithm of the employed reactive CFD solver (more details can be found in Maffei *et al.* [59] and Micale *et al.* [57]), part of the catalyticFOAM framework [55]. The catalytic source terms are included in terms of chemical source terms $\dot{s}_i$, which are, in this work, evaluated directly via the micro-kinetic model ("Direct solution MK") or via a NN surrogate ("NN surrogate").

assess its performances are introduced. Finally, the adopted benchmark cases are illustrated.

2.1. Heterogeneous chemistry in CFD

The steady-state multi-region solver, part of the catalyticFOAM framework [57] has been employed. Based on the OpenFOAM [58] environment, this solver enables the modeling of fluid flow based on the solution of the momentum, mass and energy balances in arbitrarily complex 3D domains coupled with the description of the intraparticle diffusion and reaction in the catalyst. The catalyticFOAM library is used to solve the chemistry and to evaluate thermodynamic and transport properties of the species. Additional details can be found in Maffei *et al.* [59] and Micale *et al.* [57].

Fig. 1 sketches the flowchart of the solver. At each solver iteration, the solid and gas phases are solved sequentially, starting with the fluid phase. The two phases communicate by imposing equivalence of the mass- and energy fluxes and of the mass fraction (Eq. (1)) and temperature (Eq. (2)) value at the gas–solid interface [59].

$$\omega_{i,\mathrm{fluid}}^{k} = \frac{\frac{\rho_{\mathrm{fluid}}\Gamma_{i,\mathrm{fluid}}\omega_{i,\mathrm{fluid}}^{(k-1)}}{\Delta_{\mathrm{fluid}}} + \frac{\rho_{\mathrm{solid}}\Gamma_{i,\mathrm{eff}}\omega_{i,\mathrm{solid}}^{(k-1)}}{\Delta_{\mathrm{solid}}}}{\frac{\rho_{\mathrm{fluid}}\Gamma_{i,\mathrm{fluid}}}{\Delta_{\mathrm{fluid}}} + \frac{\rho_{\mathrm{solid}}\Gamma_{i,\mathrm{eff}}}{\Delta_{\mathrm{solid}}}}; i = 1, \cdots, N_{\mathrm{G}} \tag{1}$$

$$T_{\mathrm{fluid}}^{k} = \frac{\frac{\lambda_{\mathrm{fluid}}T_{\mathrm{fluid}}^{(k-1)}}{\Delta_{\mathrm{fluid}}} + \frac{\lambda_{\mathrm{solid}}T_{\mathrm{solid}}^{(k-1)}}{\Delta_{\mathrm{solid}}}}{\frac{\lambda_{\mathrm{fluid}}}{\Delta_{\mathrm{fluid}}} + \frac{\lambda_{\mathrm{solid}}}{\Delta_{\mathrm{solid}}}} \tag{2}$$

Where ω_i^k is the mass fraction of species i and T^k is the temperature at the fluid/solid interface at iteration k, ρ is the density, Γ_i is the mass diffusion coefficient, $\Gamma_{i,\mathrm{eff}}$ is the effective mass diffusion coefficient embedding the porosity and tortuosity of the pore network, $\Delta_{\mathrm{fluid/solid}}$ are the characteristic dimensions of the fluid and the solid interface cells and λ is the mixture averaged thermal conductivity.

In a steady state solver, this procedure is iterated until the residuals of the balance equations have reached an acceptable level of convergence. During each timestep, first the species and energy convective transport are solved in the gas phase together with homogeneous reactions occurring in the system. Then, the mass and energy transport are solved together with catalytic reactions in the solid phase.

The catalytic pellets, typically composing the solid phase, are considered isotropic and modeled according to a 3D pseudo-homogeneous approach, which avoids the detailed description of the pore network inside the catalyst. Within this domain, the gaseous reactants diffuse into the porous system, adsorb, and react on the catalytic site. The steady-state species balance is described by Eq. (3) and energy balance by Eq. (4).

$$-\nabla\left(\rho\Gamma_{\mathrm{eff,i}}\,\nabla\omega_i\right) = \dot{s}_i M_i \tag{3}$$

$$-\nabla(\lambda\nabla T) = \dot{Q} \tag{4}$$

where M_i and $\dot{s}_i$ are the molar mass and the chemical source term of gas phase species i, λ is the mixture averaged thermal conductivity and $\dot{Q}$ is the reaction heat source term.

In order to solve the fields numerically and avoid unbounded solutions, the catalytic contributions in the species mass balance (Eq. (3))

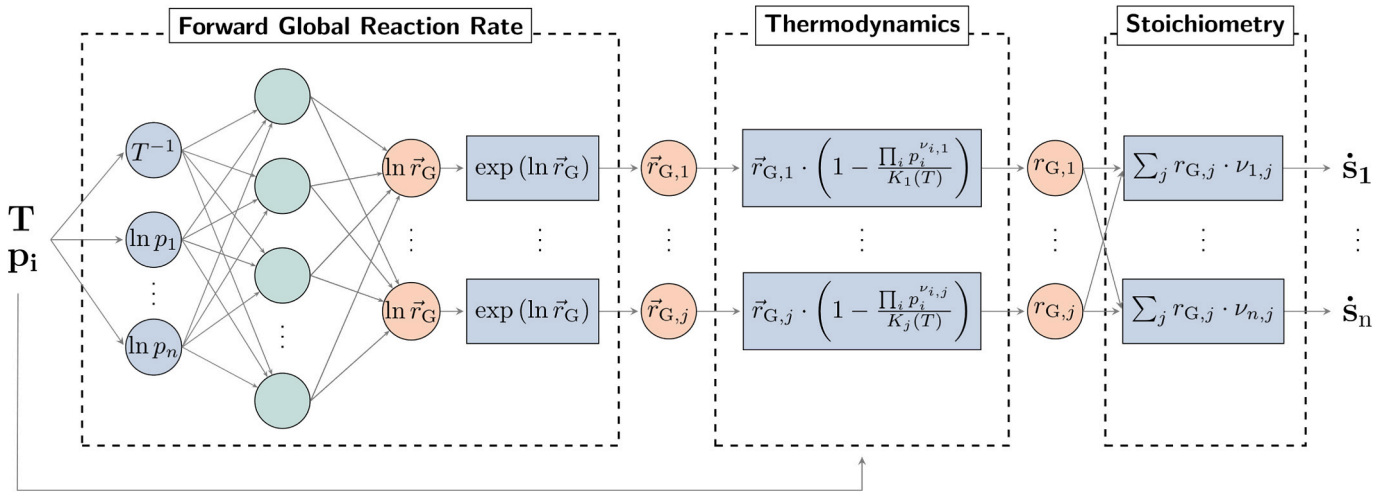

Fig. 2. Global Reaction Neural Network (GRNN) architecture with embedded stoichiometric and thermodynamic layers, as well as Arrhenius transformation [46].

and the energy balance (Eq.(4)) are linearized by a first-order Taylor expansion [57]. In the species balance, the series is developed around $\omega_{i,0}$ (Eq. (5)) and in the energy balance around T_0 (Eq. (6)). J_i is the derivative of $\dot{s}_i$ to ω_i (main diagonal Jacobians) and J_T is the derivative of $\dot{Q}$ to T (Eq. (7)).

$$-\nabla\left(\rho\Gamma_{\text{eff}}\nabla\omega_i\right) = \dot{s}_i M_i + J_i\left(\omega_i - \omega_{i,0}\right) \tag{5}$$

$$-\nabla(\lambda\nabla T) = \dot{Q} + J_T(T - T_0) \tag{6}$$

$$J_i = \frac{\partial \dot{s}_i}{\partial \omega_i};\ J_T = \frac{\partial \dot{Q}}{\partial T} \tag{7}$$

In this work, $\dot{s}_i$, J_i and J_T are evaluated either via solving the micro-kinetic scheme in-situ (*"Direct solution MK"*) or by employing a NN surrogate for catalytic rate predictions (*"NN surrogate"*). Both approaches are introduced in the following sections.

2.2. Evaluation of the catalytic source term: direct solution of micro-kinetic model

To incorporate the effects of catalytic conversion into the solution algorithm, Eq. (5) and Eq. (6) are solved in every iteration and each computational cell within a catalytically active domain. The catalytic source terms $\dot{s}_i$ are evaluated by means of the traditional micro-kinetic modeling approach. In particular, the UBI-QEP [56] based mechanism proposed by Maestri *et al.* [14], capable of describing the methane steam reforming on a Rhodium catalyst, has been selected. The original mechanism was adapted according to Kircher *et al.* [46], to ensure thermodynamic consistency with the tabulated gas phase thermodynamics from Burcat *et al.* [60]. More details are provided in the supplementary information in section S2.

In order to properly compute the source term with the micro-kinetic model, the following strategy, illustrated in Fig. 1 – *"Direct solution MK"*, is adopted [57]. In the first step, the employed micro-kinetic model is integrated numerically until a steady state solution of the surface species coverages $\vec{\theta}$ is found. This is achieved by freezing temperature and the gas-phase composition. In the second step, the gas-phase source terms $\dot{s}_i$ are evaluated using the corresponding $\vec{\theta}$. The heat source term $\dot{Q}$ is calculated via formation enthalpies and $\dot{s}_i$.

In the third step, the Jacobians J_i and J_T are evaluated numerically according to Eq. (7). The computed steady-state coverages $\vec{\theta}$ are kept constant, thus neglecting partial derivatives of the gas source terms with respect to the adsorbed species coverages. This solution strategy has been adopted to promote the stability of the segregated solution of gaseous species. However, it can slow down the solution convergence rate. Therefore, each Jacobian element has been scaled via a numerical *Jacobian Factor* (Eq. (8)), whose order of magnitude has been chosen equal to the one of the catalytic load α_{cat}.

$$J_i = \frac{J_i}{\textit{Jacobian Factor}} \tag{8}$$

In view of the Jacobian related computations, additional $N_G + 2$ source terms evaluations are required per computational cell.

Once $\dot{s}_i$, $\dot{Q}$, J_i and J_T are obtained, they are then applied to species and energy balance (Eq. (5) and (6)).

2.3. Evaluation of the catalytic source term: neural network acceleration

The acceleration of the source term evaluation via neural networks proposed in this work consists of the application of NNs for catalytic rate predictions under steady state surface conditions. The surface integration step is completed ex-situ for a number of selected conditions to generate training data. Hence, it is omitted during the CFD simulation, thus saving the most computationally expensive step in the traditional procedure, depicted in Fig. 1 and the "*Direct solution MK*" (step 1).

The "*NN surrogate*" scheme in Fig. 1 shows the proposed NN accelerated solution strategy, to be applied in each catalytic computational cell (catalyst domain) at each iteration. In the first step, temperatures T and the gas phase compositions p_i of numerous computational cells are iteratively gathered in mini batches and passed to the NN as input/features. The NN then predicts the catalytic source terms $\dot{s}_i$ under steady-state surface conditions and returns the values as output/targets to catalyticFOAM. The whole procedure continues until $\dot{s}_i$ is evaluated for all the catalytically active fields. In step two, the heat source term $\dot{Q}_i$ is evaluated using $\dot{s}_i$ and the formation enthalpies.

It is worth noting that the implementation via mini-batches enables the adoption of optimized matrix operations, thus enhancing performance and allowing for a future more efficient application of the NN-accelerated approach on GPUs.

In the third step, the Jacobians J_i and J_T (Eq. (7)) are evaluated numerically, thus requiring additional $N_G + 2$ source term evaluations. In contrast to the last section and the "*Direct solution of MK*" approach, due to the design of the NN surrogate described here, the evaluated Jacobians are always under steady-state surface conditions. The influence on the convergence behavior of the solver will be examined in more detail in a subsequent study. Further, it is worth noting that NNs are continuous and fully differentiable functions. Therefore, J_i could be evaluated even more efficiently and accurately using analytical

derivatives of the neural network in the future.

To employ NNs of arbitrary architecture in catalyticFOAM, an API to ONNX runtime [61] has been developed. The API is embedded into catalyticFOAM and accepts settings in the traditional OpenFOAM *dictionary* format. It can load and run any NN model, such as the GRNN architecture, with the *Open Neural Network Exchange* (ONNX) format. Thus, a machine learning model can be developed in most of the programming environments and frameworks, as they commonly provide an export function. Extrapolation strategies, for example when predicting rates outside the training space, can be implemented and exported to the surrogate model as well. However, no extrapolation strategy has been implemented in this work. Furthermore, the number of ML models employed in one simulation/region is not limited, offering high flexibility for research and production.

2.4. Global reaction neural network (GRNN)

In this work, a single GRNN [46] is employed as surrogate model for catalytic rate prediction for the kinetic mechanism over the entire range of conditions present in CFD simulations for a wide range of inlet conditions.

The architecture design is illustrated in Fig. 2. It is comprised of three sections. The first section, designated as "*Forward Global Reaction Rate*", is a feed-forward neural network with trainable parameters w (weights) and b (biases). Its objective is to provide a latent description of all global forward rates $\vec{r}_{G,j}$ of a system. Furthermore, it incorporates chemical knowledge regarding the Arrhenius law by scaling the input parameters accordingly ($\ln(p_i)$, $1/T$). The second section, designated as "*Thermodynamics*", evaluates the global net-rates $r^{net}_{G,j}$ via the De Donder Equation [62] (Eq. (9)). In the final section, "*Stoichiometry*", $\dot{s}_i$ is calculated via the stoichiometric matrix (Eq. (10)) and thus ensures mass conservation.

$$r^{net}_{G,j} = \vec{r}_{G,j}\left(1 - \frac{\Pi_i (p_i/p_0)^{\nu_{i,j}}}{K_j}\right) \tag{9}$$

$$\dot{s}_i = \sum\nolimits_j \nu_{i,j} r_j = GRNN(p_i, T) \tag{10}$$

By design, a set of global reactions must be selected for a given system. In the context of steam reforming, the global reactions are:

$CH_4 + H_2O \rightleftharpoons 3H_2 + CO$	R1: Steam Reforming
$H_2 + CO_2 \rightleftharpoons H_2O + CO$	R2: Water-Gas Shift
$CH_4 + 2H_2O \rightleftharpoons 4H_2 + CO_2$	R3: Direct-Reforming

The GRNN employed in this work is trained to predict gas phase source terms $\dot{s}_i$ (Eq. (10)) under steady state surface conditions for the gas reactants in MSR (H_2, H_2O, CO, CO_2, CH_4).

For ex-situ training and validation of the GRNN, a dataset for source term prediction is generated. A set of conditions is sampled uniformly in their respective scaled space: reciprocal or logarithmic. We sample the temperature T, conversion X_{CH_4}, the selectivity S_{CO}, the steam-to-carbon ratio and the total pressure within ranges present in the MSR regime. By using these values and a simple PFR model with the original microkinetics, a dataset of gas phase compositions is obtained. By doing so, all sampled data points are ensured to be representative of the conditions in the studied process. Furthermore, to account for eventual deviations from such ideal compositions, e.g., due to diffusion effects, 10 % of gaussian noise is applied to the finally sampled partial pressures. For each set of partial pressures and temperature, $\dot{s}_i$ are evaluated under steady state $\vec{\theta}$, as described in Section 2.2. For the evaluation of the corresponding source terms, we have used the OpenSMOKE++ framework [63], the same that is implemented in the employed CFD solver, to solve for the corresponding source terms. The dataset is then split into a training dataset (25 %), a validation dataset (25 %) and a test dataset (50 %). The model is optimized on the training dataset. During the training process, the validation dataset is utilized after every ten iterations to assess the model's ability to generalize on the task at hand. Finally, the test dataset is employed for evaluating and comparing fully trained models. The ranges are provided in Table 1.

Table 1
Range of sampled temperature, conversion, selectivity, steam-to-carbon ratio and total pressure for MSR.

Inlet conditions	Unit	Minimum	Maximum	Scaling
T	K	780	1120	reciprocal
X_{CH_4}	–	0.02	0.99	logarithmic
S_{CO}	–	0.05	0.50	logarithmic
$r_{steam\_to\_carbon}$	–	3.0	4.0	logarithmic
p	bara	6.0	8.0	logarithmic

The GRNN training procedure is adopted from the work of Kircher *et al.* [46] and it is implemented in Pytorch v2.1. Weights are initialized by *Xavier* [64] initialization, a common strategy that aims for exploding or vanishing gradients in the beginning of the training. Features are scaled by min–max scaling between −1 and 1. The model is trained using the LBFGS optimizer to minimize the root-mean squared relative error of predicted chemical source terms. During the training, the performance is continuously evaluated on the validation dataset and the model with the best performance on the validation set is saved. The results of the training procedure are discussed in Section 3.1.

The implemetation for training of GRNN surrogates for a detailed micro-kinetic model can be found on our github page: https://github.com/VotsmeierGroup/GlobalReactionNeuralNetwork.

2.5. Packed-bed reactor models

A lab- and an industrial 3D-reactor case have been selected to showcase the applications of GRNNs in catalytic CFD simulations. In both, the flow is assumed to be laminar. The packed bed geometries were created with the software Blender 2.79, following the methodology proposed by Partopour & Dixon [65].

The lab (scale) reactor, is presented in Fig. 3.a. It has a diameter of 2.54 cm. The industrial (scale) reactor is shown in Fig. 3.b and has a diameter of 10.28 cm, which is based on the work of Plehiers & Froment [66]. Both reactors models were meshed with snappyHexMesh [67]. The algorithm of the meshing software snaps a base mesh to fit the dimensions of any provided boundaries. For multi-region meshes, this strategy ensures conformation for the interface cells of the meshes but it may lead to coarser representation of surfaces. Regardless, the proposed methodology is independent of the mesh. For both, a refinement across the surface of minimum level two and maximum level three with three cells between levels was applied. The lab reactor consists of a total of 2.34 million computational cells (min. volume = 4.4e-12 m^3), of which 41 % represent the solid reactive phase. The industrial reactor has been meshed with a total of 44.75 million cells (min. volume = 7.1e-13 m^3), of which 54 % constitutes the reactive phase. Information regarding the reactor geometry and catalyst properties is listed in Table 2.

Gas phase reactions are not considered, neither in the fluid region nor within the porous pellets. At the inlet, a *Dirichlet* boundary condition is applied for species, inlet flow and fluid temperature. The values are in Table 3 together with the reactor operating conditions. At the outlet, *Neumann* conditions (zero gradient) are applied for all variables, besides pressure.

At the interface between the fluid phase and the pellets, equal fluxes and values are ensured, as discussed in the work of Maffei *et al.* [59]. At the wall, a similar approach for equal heat fluxes is chosen with the only difference, that a constant temperature T_{wall} is assumed at the outside of the reactor tube. The boundary temperature T_B at the tube interface is calculated as:

$$T_B = \frac{h_{wall} T_{wall} + \frac{\lambda_{fluid} T_{fluid}}{\Delta_{fluid}}}{h_{wall} + \frac{\lambda_{fluid}}{\Delta_{fluid}}} \tag{11}$$

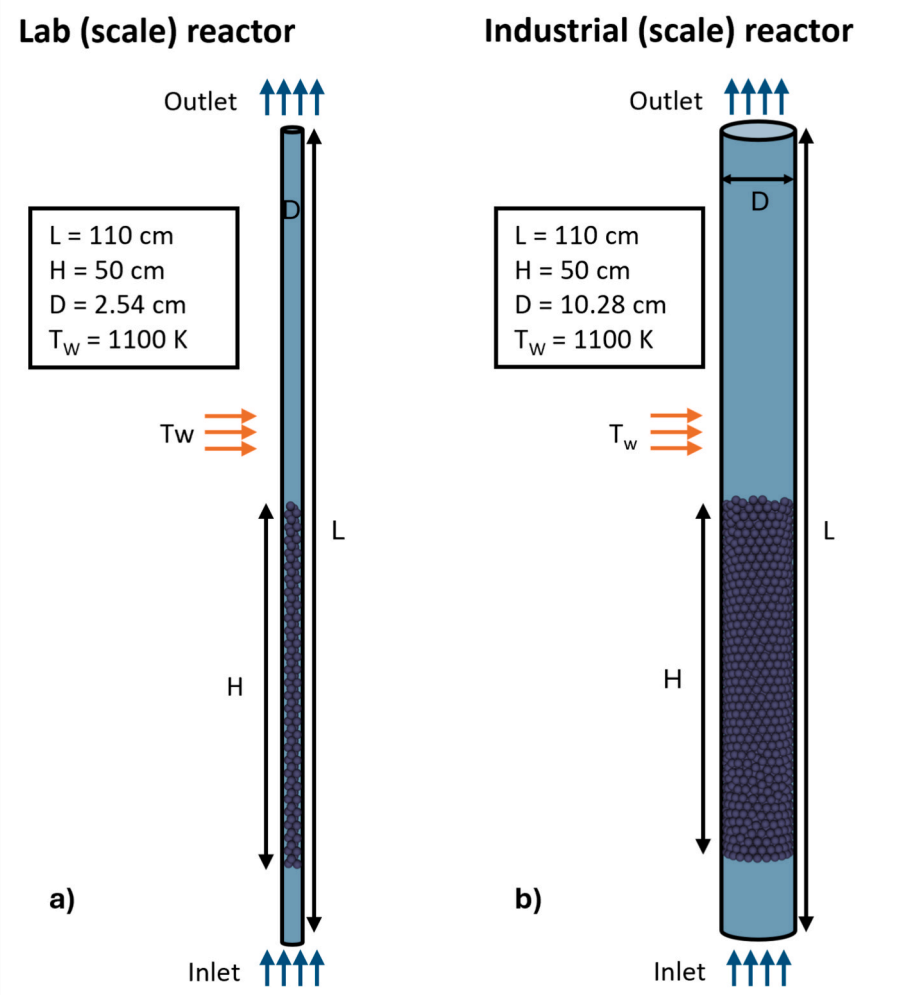

Fig. 3. Geometry and the boundary names of both 3D-reactor cases employed in this work. The lab reactor in a) and the industrial reactor in b). Details of both geometries and catalyst properties are listed in Table 2.

Table 2
Reactor geometries and catalyst properties of MSR on Rh.

	lab reactor	industrial reactor	Unit
Reactor geometry			
Reactor diameter	2.54	10.28	cm
Reactor length	110		cm
Reactor wall diameter [66]	3.1		cm
Catalytic bed length	50		cm
Pellet diameter	1.27		cm
Number of pellets	~ 110	~ 2400	–
Catalyst properties			
Catalytic load α_{cat}	1000		m^2_{cat}/m^3_{cat}
Porosity ϵ_p	0.5		–
Tortuosity τ_p	5		–
Conductivity λ_{solid}	2.5		W/(m·K)

Table 3
Inlet boundary and operating conditions.

Inlet Composition			
H_2O [mole/mole]	0.5	H_2 [mole/mole]	0.004
CH_4 [mole/mole]	0.15	CO_2 [mole/mole]	0.0025
N_2 [mole/mole]	0.3439	CO [mole/mole]	0.0006
Operating conditions			
T_{wall} [K]	1100	p [bara]	10
T_{in} [K]	793	u_{in} [m/s]	0.05–1

with the thermal heat-transfer coefficient h_{wall} (Eq. (12)) of the tube, the thermal conductivity λ_{fluid} of the fluid and the cell-center-to-interface distance Δ_{fluid} [66].

$$h_{wall} = 10.738 + 0.0242 \cdot \frac{T_{wall} - T_{fluid}}{2d_{wall}} \tag{12}$$

To ensure the optimal utilization of computational resources, a scalability study was conducted with both reactor models. The objective was to identify the maximum number of CPUs that could be utilized while maintaining a parallelization efficiency of over 85 %. For the industrial reactor, the optimal utilization is achieved through the employment of 16 CPUs and the decomposition of the computational mesh using the "scotch" method. It should be noted, however, that the lab reactor is operated with either the "Direct solution MK" approach or the GRNN surrogate (see Section 2.1). The scalability study demonstrated that the parallelization efficiency declines more rapidly with the GRNN surrogate than with the in-situ full evaluation of the micro-kinetic scheme. Consequently, the resource allocation strategy that exhibited the least discrepancy in efficiencies was selected, namely the employment of nine CPUs and the "simple" decomposition strategy. *Dynamic load balancing*, as proposed by Micale *et al.* [68], may represent a potential strategy to further enhance the parallelization efficiency. More details on the scalability study are provided in the supplementary information section S1.

2.6. Neural network performance metrics

This section introduces metrics to evaluate the accuracy and speed-up provided by the GRNN accelerated approach for the catalytic source term evaluation. Depending on the metrics, they have been applied either to the CFD simulations or during the NN training phase.

The accuracy of a prediction of the GRNN (denoted by "^") is either evaluated by the deviations of the mole fractions χ_i of the converged solutions ϵ_{MF} or deviations of chemical source terms $\epsilon_{\dot{s}}$ against the corresponding reference. ϵ_{MF} is adopted only in the case of CFD simulations and is calculated via Eq. (13), where N_{cells} is the total amount of computational cells in the pellet domain. Cells with χ_i smaller than the threshold of $1{\cdot}10^{-6}$ are neglected to suppress the influence of numerical fluctuations.

$$\epsilon_{MF} = \frac{1}{2{\cdot}N_{\text{cells}}} \cdot \sum_{j}^{N_{\text{cells}}} \sum_{i}^{\{CH_4,CO\}} \left(\frac{\chi_i - \widehat{\chi}_i}{\chi_i} \right) \tag{13}$$

$\epsilon_{\dot{s}}$ is used both for evaluation during training and to evaluate the accuracy of a CFD simulation run with the GRNN model and is calculated via Eq. (14). In the latter case, the amount of datapoints N becomes N_{cells}.

$$\epsilon_{\dot{s}} = \frac{1}{n{\cdot}N} \cdot \sum_{j=1}^{N} \sum_{I=1}^{n} \left(\frac{\dot{s}_{i,j} - \widehat{\dot{s}}_{i,j}}{\dot{s}_{i,j}} \right) \tag{14}$$

Finally, ϵ_{MF} and $\epsilon_{\dot{s}}$ has been also computed for each catalytic computational cell, leading to their local forms, $\epsilon_{\text{MF,loc}}$ and $\epsilon_{\dot{s},\text{loc}}$, whose expression is reported in Eq. (15) and Eq. (16). In the local representation, no threshold is applied.

$$\epsilon_{\text{MF,loc}} = \frac{1}{2} \cdot \sum_{i}^{\{CH_4,CO\}} \left(\frac{\chi_i - \widehat{\chi}_i}{\chi_i} \right) \tag{15}$$

$$\epsilon_{\dot{s},\text{loc}} = \frac{1}{n} \cdot \sum_{i=1}^{n} \left(\frac{\dot{s}_i - \widehat{\dot{s}}_i}{\dot{s}_i} \right) \tag{16}$$

For a complete comparison, the selectivities, S_{CO} and S_{CO2}, resulting from the MSR reaction network are discussed in terms of M_{module}, which can be used to specify the stoichiometry of the produced syngas:

$$M_{\text{module}} = \frac{H_2 - CO_2}{CO + CO_2} \tag{17}$$

The speed-up is assessed with two measurements. Firstly, by the *total simulation speed-up* (Eq. (18)) and secondly, for a more detailed investigation, by the *chemistry speed-up* of the related sub-solution step of the algorithm (Eq. (19)).

$$total\ speed-up = \frac{total\ simulation\ time - reference}{total\ simulation\ time} \tag{18}$$

$$chemistry\ speed-up = \frac{chemistry\ step\ evaluation\ time - reference}{chemistry\ step\ evaluation\ time} \tag{19}$$

With full evaluation of the micro-kinetic scheme, the chemistry sub-solution includes accessing all relevant data, e.g. gas phase composition and temperature, of every computational cell, solving the ODE equations and the evaluation of $\dot{s}_i$ for the gas phase species. In the case of the use of an NN surrogate, the ODE integration step is omitted.

The *total speed-up* provides valuable information for the individual application. It includes all sub steps of the CFD solver, e.g. solving the fluid temperature field. Its value is strongly dependent on the reactor case and the chosen conditions. For the sake of clarity, all computational overheads, such as mesh decomposition for parallelization or memory allocation for the individual fields are excluded in the evaluation of the *total speed-up*. The benchmark starts with the iteration loop of the solver.

The *chemistry speed-up,* however, provides insight into the actual impact of employing NNs in reactive CFD, while excluding all parts of the algorithm that are unrelated to the evaluation of the catalytic source terms. However, it is worth noting that, if the amount of gas phase species can be reduced due to an applied NN surrogate, it would also increase the *total speed-up* due to omitting solving the transport of them in each region and thus, would not be measured in the *chemistry speed-up*.

3. Results and discussion

The following section discusses the Global Reaction Neural Network (GRNN) training and examines the application of GRNNs as surrogate models in reactive CFD on the lab and the industrial reactor. The lab reactor is run both with full evaluation of the micro-kinetic scheme and a GRNN surrogate. The results obtained from the full evaluation of the micro-kinetic scheme are presented here as a reference for assessing accuracy and speed-up. Furthermore, the application range of a single GRNN surrogate model is examined. Subsequently, the industrial reactor model is employed and studied accordingly. Finally, to showcase the benefits of the proposed methodology and the provided speed-up, both reactors are compared at the same mass-based space-velocity *GHSV* (related to standard conditions 273.15 K/ 1 atm).

The simulations were carried out on the high-performance computer Lichtenberg at the NHR Centers NHR4CES at TU Darmstadt. The base CPU frequency is 2.1 GHz. All simulations were run until convergence was reached in all properties (residuals $< 1{\cdot}10^{-5}$). Unless otherwise stated, the catalyst was always initialized as empty and the velocity field in the fluid domain was always initialized with zero for all directions. All the other fields were initialized according to the inlet conditions. For more information about initializing the surface coverages, see supplementary information section S2.1.

3.1. GRNN training

The training procedure is described in Section 2.4, mostly following the work of Kircher. *et al.* [46]. The target for the model was a relative error in predicted source terms $\epsilon_{\dot{s}} \approx 0.1\%$ on the training dataset. In preliminary studies, the amount of required trainings data and the architecture was studied rigorously. We found that between 2,000–10,000 data points were sufficient to reach the target accuracy. The final training, validation and test datasets in this work contain 10,000, 10,000 and 20,000 data points, respectively. Combined, approximately 15 s were required for the evaluation of the 40,000 steady state source terms.

In this study, an architecture with 3 layers with 60 nodes per layer with hyperbolic tangent activation functions in the hidden layers was found to be optimal. The optimal architecture is determined by providing a sufficient number of trainable parameters to the model, to reach the required accuracy, while avoiding an increase in training and in-production prediction times. Finding the optimal architecture or rather hyperparameters is a case-specific optimization procedure [69]. The entire training process for the GRNN surrogate took 22 h on three CPUs on our cluster. For clarity, the training time is highly dependent on the size of the training dataset and the number of tunable parameters. However, no methods or functions were compiled, which could be used to further decrease the computational time.

Fig. 4a shows the loss $\epsilon_{\dot{s}}$ (Eq. (14)) of the GRNN on the training and the validation data against the epochs/iterations during the training procedure. Both the training and validation errors decline steadily. Since $\epsilon_{\dot{s}}$ on the validation dataset has not yet reached its minimum, the number of epochs can be extended. However, after about 10,000 epochs, the GRNN reaches a value for $\epsilon_{\dot{s}}$ of 0.08 % on the training data and 0.21 % on the validation data, which was considered sufficient for the application purpose.

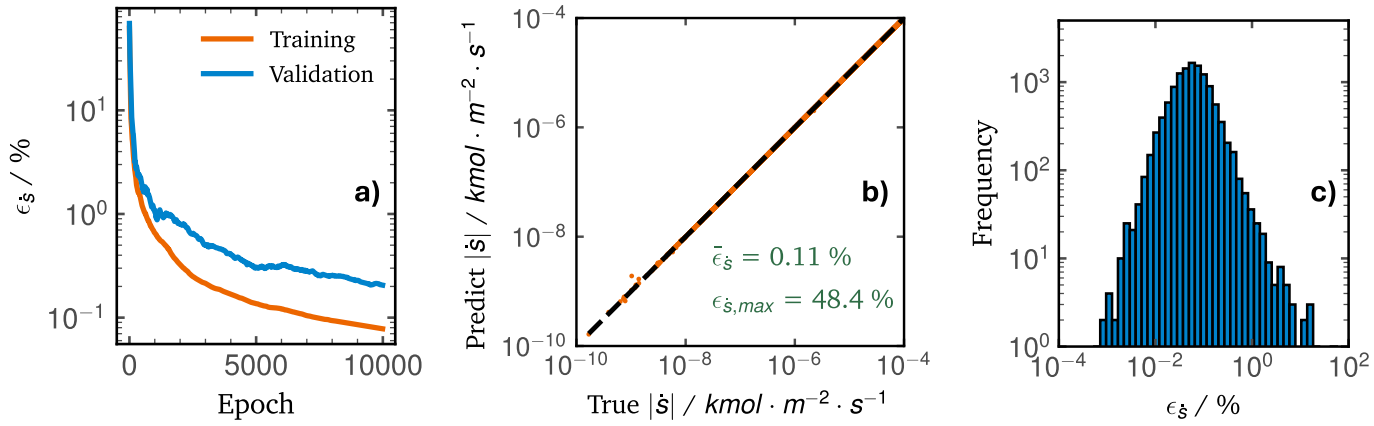

Fig. 4. Training of the GRNN: relative error $\epsilon_{\dot{s}}$ in the source term predicted by the GRNN on the training and validation datasets (a), parity of the GRNN predictions on the test dataset against the corresponding ground truth chemical source terms (b), histogram of $\epsilon_{\dot{s}}$ on the test dataset (c).

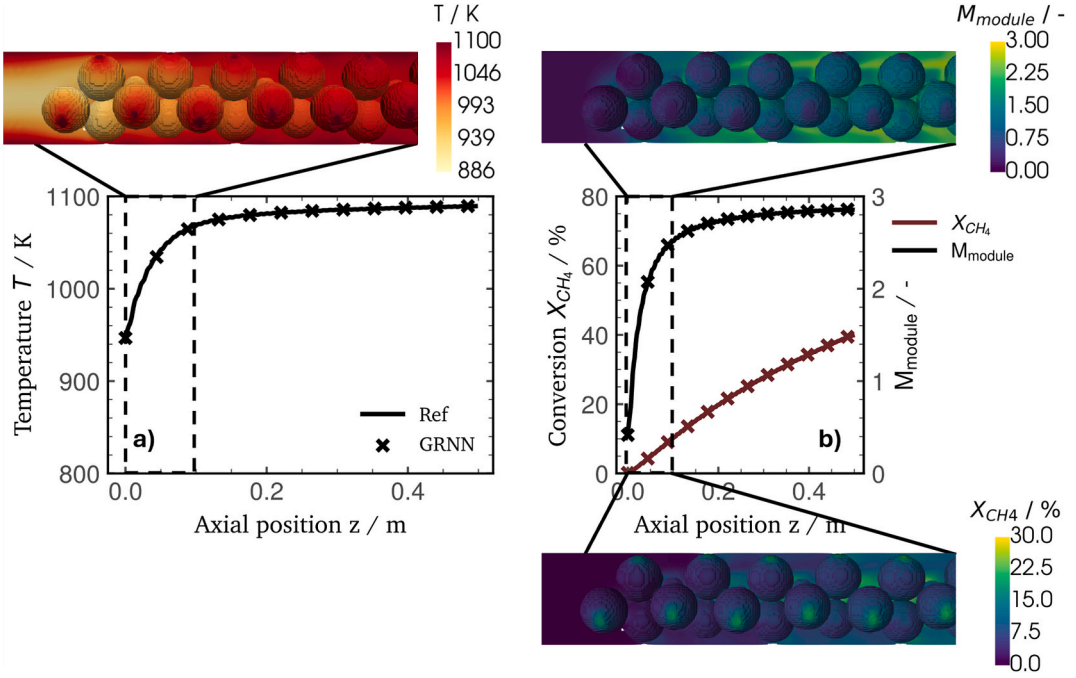

Fig. 5. Result of the lab reactor run with conditions listed in Table 3 and $U_{in} = 0.1\,m\,s^{-1}$. In the center: In a) the cup-mix of T, in b) the cup-mix of X_{CH4} and the M_{module} (Eq. (17)). On top and on the bottom are parts ($z > 0$, $z < 0.1$ m) of the respective fields visualized from the solution with employed GRNN. The solid line belongs to the reference, the cross markings the solution with the GRNN model as surrogate.

Fig. 4b shows the parity plot of the GRNN predictions on the test dataset against the corresponding ground truth chemical source terms. The predictions match their corresponding reference in all orders of magnitude well. However, a few outliers can be found for $|\dot{s}|$ smaller than $1{\cdot}10^{-8}\,kmol\,m^{-2}\,s^{-1}$. Fig. 4.c shows $\epsilon_{\dot{s}}$ on the test dataset as a histogram. For the majority of datapoints, $\epsilon_{\dot{s}}$ is below 0.1 %, only showing a few outliers $\epsilon_{\dot{s}}$. On average, $\epsilon_{\dot{s}}$ on the test dataset is 0.11 %.

3.2. Lab reactor

The lab reactor was always simulated twice under the conditions listed in Table 3 and the respective inlet velocity U_{in}. Once with the full evaluation of the micro-kinetic scheme, the reference in this work, and once using the GRNN surrogate model. All simulations with full evaluation of the micro-kinetic scheme represented in this section use empty catalytic sites as initial surface state (see supplementary information section S2.1). Fig. 5 compares both solutions of the lab reactor at an inlet velocity $U_{in} = 0.1\,m\,s^{-1}$ as plots of the cup-mix average temperature T in a) and the conversion X_{CH4} and the M module M_{module} (Eq. (17)) in b) against z. Slices of the respective fluid fields together with the pellets at the beginning of the packed bed ($0 < z < 0.1$ m) are visualized as well.

The solid lines in Fig. 5 are evaluated from the reference solution. The symbols show the solution obtained by the GRNN-accelerated model. Axial temperature, X_{CH4} and M_{module} profiles obtained with the GRNN exhibit a high degree of qualitative alignment with the reference data. The X_{CH4} profile indicates that the reactive system has not reached its equilibrium yet, as it is steadily increasing.

It is also interesting to note that the selected operating conditions correspond to a reactor operated in partial mass transfer limited regimes (averaged bed efficiency η_{bed} [59] = 0.53), thus, highlighting the effectiveness of the coupling between the transport phenomena and the rates evaluated via the GRNN. For a more quantitative analysis, in Fig. 6 local deviations between the reference solution and the solution with the GRNN are shown. In Fig. 6.a radial profiles of three selected pellets in

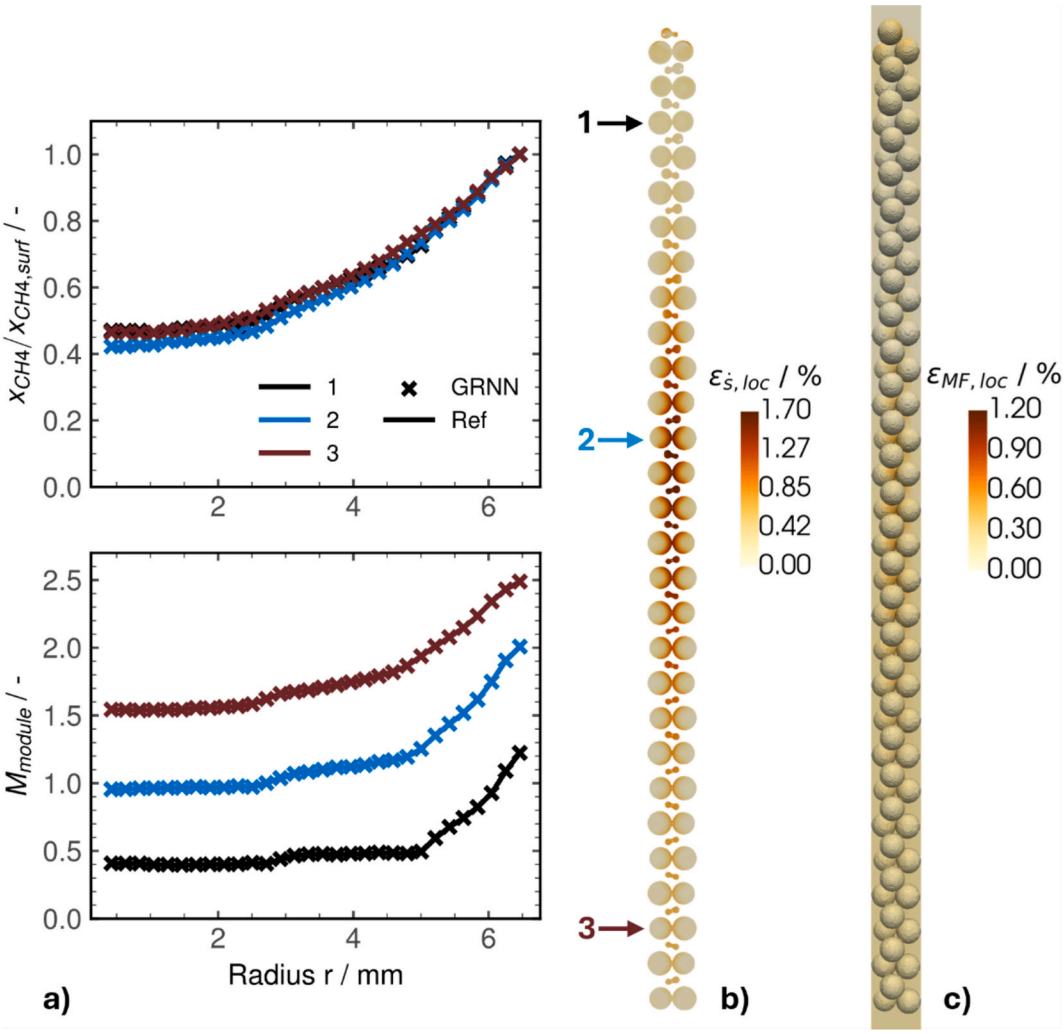

Fig. 6. The normalized mole fraction $\chi_{CH_4}/\chi_{CH4,surf}$ (top) and the M_{module} (bottom) against the radius r in three selected pellets in a). The solid line belongs to the reference, the cross markings the solution with the GRNN model as surrogate. The local deviation $\epsilon_{\dot{s},loc}$ (Eq. (16)) in b) and $\epsilon_{MF,loc}$ (Eq. (15)) in c) of the converged simulation with applied GRNN surrogate against its reference with the lab reactor run with the conditions listed in Table 3 and with $U_{in} = 0.1\,m\,s^{-1}$.

different locations in the reactor are plotted. In the upper plot, the average mole fraction χ_{CH_4} normalized with the surface mole fraction $\chi_{CH4,surf}$ and on the bottom, the M_{module} is plotted against the radius r of the respective pellet. The radial profiles of the selected pellets and both solutions visually align well. For a quantification of deviations between both entire simulations, the catalytic source terms $\epsilon_{\dot{s},loc}$ (Eq. (16)) and the local deviation of the mole fractions $\epsilon_{MF,loc}$ (Eq. (15)) are shown in Fig. 6 in b) and c), respectively.

The pellet domain is shown as an axial slice in Fig. 6.b, while Fig. 6.c depicts an axial slice of the fluid domain along with the three-dimensional pellet domain. In general, the rates deviate the most in the center of the tube and around the second third of the reactor axis with a maximum value of $\epsilon_{\dot{s},loc}$ is 1.68 %. Interestingly, the deviations in the first and third sections are significantly smaller (< 1.0 %). The local maxima cannot therefore be attributed to error propagation alone. The compositions in these areas are also always within the training ranges of the GRNN (see Table 1). Extrapolation can therefore be ruled out as a source of error. In the second third of the bed, the temperature in the center of the bed has risen close to the heated wall temperature (see Fig. 5.a), but a significant amount of the reactants have not been converted yet. A plausible explanation for the increased prediction error could be the design of the training dataset. It was created by sampling along PFR-like trajectories and applying Gaussian noise to account for

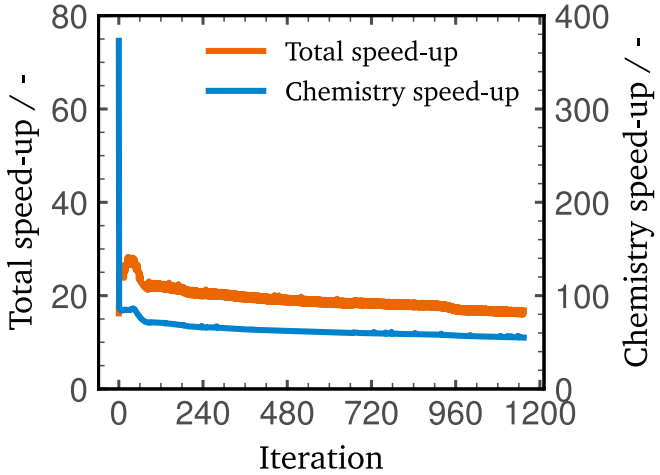

Fig. 7. *Total speed-up* (Eq. (18)) and *chemistry speed-up* (Eq. (19)) of the solver against the iteration. Compared are simulations with the lab reactor run under reference conditions (see Table 3) with $U_{in} = 0.1\,m\,s^{-1}$.

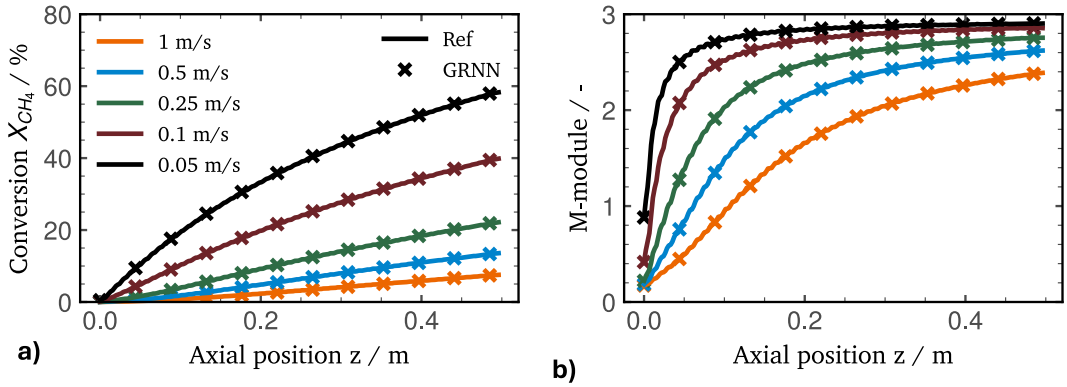

Fig. 8. Cup-mix of X_{CH4} in a) and M_{module} (Eq. (17)) in b) plotted against the axial position z from converged solution of the lab reactor run under the conditions listed in Table 3 and $U_{in} = \{0.05, 0.1, 0.25, 0.5, 1\}\,m\,s^{-1}$. The solid line belongs to the reference, the cross markings to the solution with the GRNN model as surrogate.

diffusion in CFD simulations. It is therefore likely that areas with low conversion but high temperature in the multi-dimensional space are under-represented in the training dataset and hence, that predictions with the GRNN are slightly less accurate there. A higher representation of such a regime in the training dataset can potentially improve the accuracy. Another approach to avoid decreased local accuracies can be to employ a machine learning mode that can estimate the prediction error and be retrained on-the-fly [38,41]. Nevertheless, the average deviation $\epsilon_{\dot{s}}$ is 0.49 %, resulting in a negligible overall effect on the reactor behavior. Not surprisingly, high $\epsilon_{MF,\,loc}$ can be found at areas with relatively high $\epsilon_{\dot{s},loc}$. The highest $\epsilon_{MF,\,loc}$ is however 1.16 %. On average, the deviation of the mole fraction fields ϵ_{MF} is 0.23 %. The simulation with the GRNN thus replicates the chemical evolution of the system well.

Fig. 7 illustrates the *total speed-up* (Eq. (18)) and the *chemistry speed-up* (Eq. (19)) observed when employing the GRNN surrogate over the full evaluation of the micro-kinetic scheme for the lab reactor with $U_{in} = 0.1\,m\,s^{-1}$.

In the initial iteration, the largest *total speed-up* and the largest *chemistry speed-up* are 28.2 and 373.1, respectively. Thereafter, both trends decline rapidly at the beginning and then very slowly reach a *total speed-up* of approximately 17 and a *chemistry speed-up* around 55. The computational cost for the source term evaluation can be assumed to be constant in both approaches. The initial large speed-up can be attributed to the initial guess of the surface composition, which in this case was an empty catalyst, making the ODE solution in the first step more computationally expensive. As the simulation progresses and the previous solutions for the surface coverages $\vec{\theta}$ provide increasingly better values for the current iteration, the computational time for a single iteration step decreases for the reference case. An average *chemistry speed-up* of 63.1 and an average *total-speed-up* of 19.2 are obtained.

In absolute terms, with full evaluation of the micro-kinetic scheme, $(287.11 \pm 51.64)\,\mu s$ were required on average to obtain steady state source terms for each computational cell. The computational time for the entire simulation was approximately 114 h on four CPUs on our cluster, with 96.3 % of the computational cost allocated to the chemistry sub-step. With employed GRNN, the average prediction time for source terms per computational cell was reduced to 4.55 µs. The total simulation time was 6 h on the same number of CPUs. The chemistry sub-step accounted for 29.2 % of the total computational cost. Consequently, approximately 1.75 h of the full 6 h were allocated to evaluate catalytic source terms. It can be concluded that with the proposed methodology the primary bottleneck of the simulation is no longer the source term evaluation. In order to increase the speed-up significantly, solving the transport has to be optimized. Employing machine learning models for this task might be an option [70–72].

It should be noted that the observed speed-up depends on the conversion achieved in the reactor and on the complexity/stiffness of the micro-kinetic scheme. The higher the reactivity/conversion, the more computational time is required to solve the full micro-kinetic scheme, and more iterations are required to reach a convergence. The total simulation time of the "*Direct solution MK*" approach is thus proportional to the mass-based space-velocity *GHSV*. However, the prediction time of the GRNN model remains constant. Therefore, *total speed-up* increases as the *GHSV* increases.

Table 4
Results and accuracy, measured as ϵ_{MF} (13) and $\epsilon_{\dot{s}}$ (14), obtained with the lab reactor under reference conditions (see Table 3) and for different inlet velocities U_{in}.

	U_{in} [m/s]				
	1.00	**0.50**	**0.25**	**0.10**	**0.05**
GHSV $\left[m^3_{gas} kg^{-1}_{cat} h^{-1}\right]$	101.6	50.8	25.4	10.2	5.1
$X_{CH_4,out}$ [%]	7.5	13.5	22.3	40.1	58.7
ϵ_{MF} [%]	0.18	0.13	0.08	0.23	0.35
$\epsilon_{\dot{s}}$ [%]	0.38	0.30	0.25	0.49	0.78

To demonstrate the versatility of a single GRNN model, a series of simulations was conducted with varying inlet velocities ($U_{in} = \{0.05, 0.1, 0.25, 0.5, 1\}\,m\,s^{-1}$). This approach allowed for the variation of the residence time, temperature field, and conversion within the reactor model. In Fig. 8, the cup-mix profiles of X_{CH4} (left) and M_{module} (right) are represented against the axial position z. The solid lines represent the converged results of the reference cases, and the cross marking of the solutions with the applied GRNN surrogate.

In Table 4, $X_{CH_4,out}$, η_{bed}, ϵ_{MF}, $\epsilon_{\dot{s}}$ and the space-velocity *GHSV* are listed together with the corresponding U_{in}. While the operating conditions and thus the conversion differ ($X_{CH_4,out}$ reaches values between 7.5 and 58.7 %), the accuracy of the NN-enhanced simulations with the GRNN surrogate is such that $\epsilon_{MF} << 1\%$ and $\epsilon_{MF,loc,\,max}$ 1%, as well as $\epsilon_{\dot{s}} < 1\%$ and $\epsilon_{\dot{s},\,loc,\,max}$ 2%. Thus, the GRNN model generalizes well over the investigated range of operating conditions. Due to the observed *total speed*-up, it represents a valuable enhancement for particle resolved CFD.

3.3. Simulation of an industrial scale reactor

In the following the solution of the industrial reactor, obtained under conditions listed in Table 3 and with an inlet velocity $U_{in} = 0.1\,m\,s^{-1}$ is analyzed and discussed. Due to the dimensions of the reactor model, a converged solution with full evaluation of the micro-kinetic scheme is not viable. Therefore, the following illustrations from the converged fields are from the employed GRNN.

The converged solution is shown in Fig. 9. The figure depicts the cup-

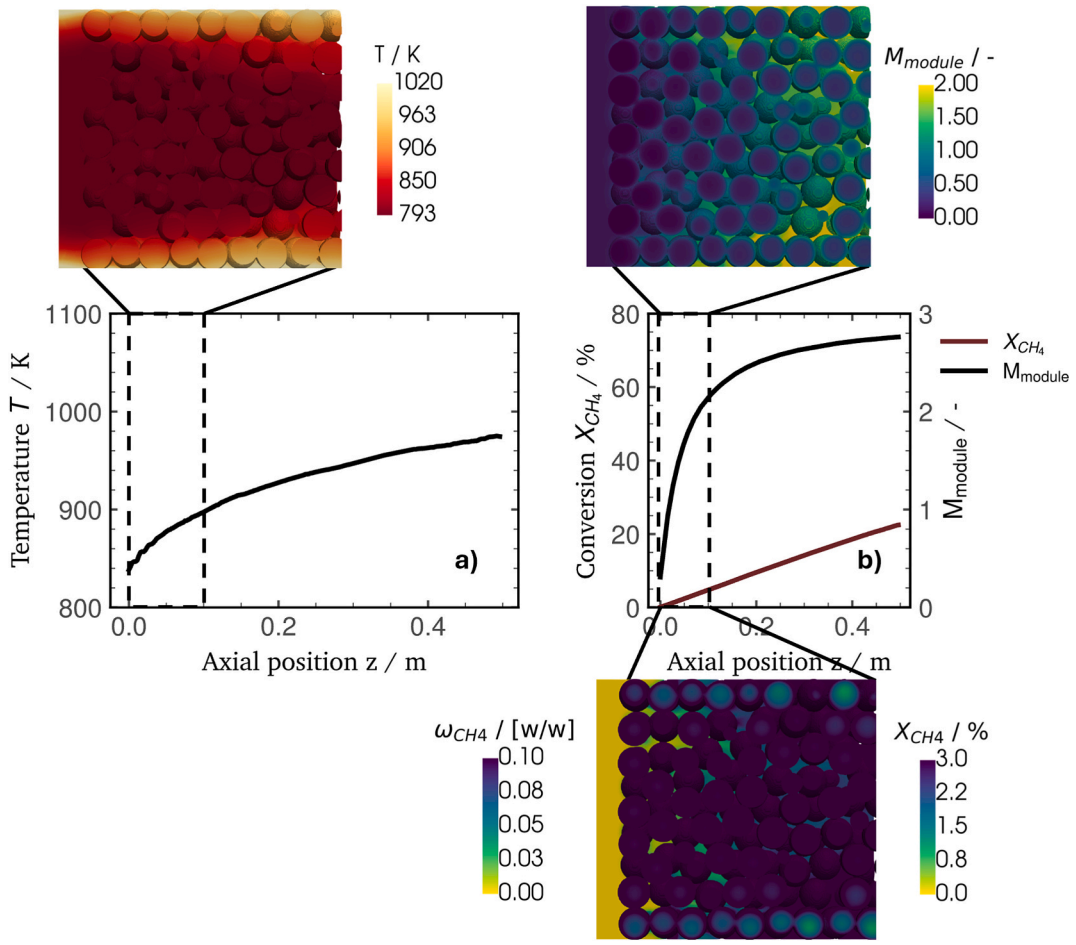

Fig. 9. Cup-mix of the temperature against z in a) and the cup-mix of M_{module} (Eq. (17)) and X_{CH4} against z in b). For each cup-mix a zoomed and sliced view of the corresponding fields ($0\,m > z > 0.1\,m$) is added. In the sliced view in the bottom right, in the fields of the pellets, the mass fraction ω_{CH4} is color-coded. The results are from the solution of the industrial reactor with employed GRNN under conditions listed in Table 3 with $U_{in} = 0.1\,m\,s^{-1}$.

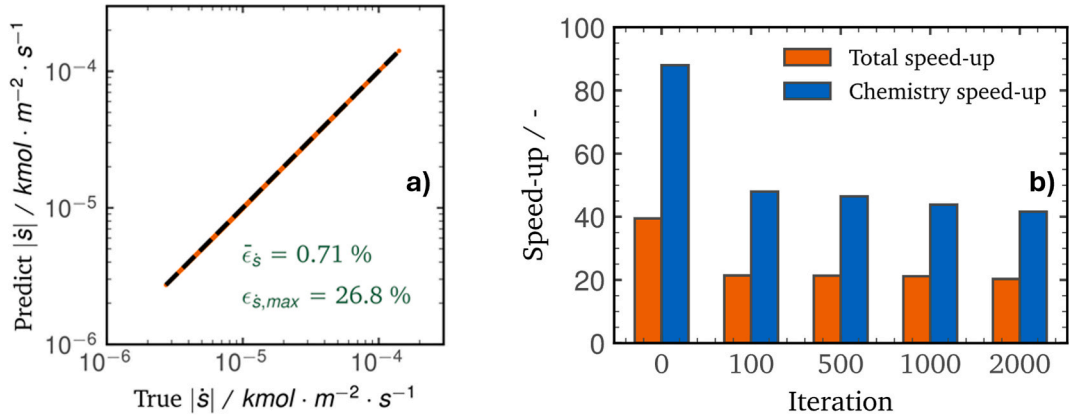

Fig. 10. In a) the parity plot of true and predicted $|\dot{s}|$ is shown. The rates were evaluated for a randomly selected subset of compositions found in the pellet domain of the converged solution. Both $\bar{\epsilon}_{\dot{s}}$ and $\epsilon_{\dot{s},max}$ are evaluated with a threshold of $\dot{s}_i < 1{\cdot}10^{-8}\,kmol{\cdot}m^{-2}\,s^{-1}$. In b), the discrete *total speed-up* and the *chemistry speed-up* are shown in a bar diagram.

mix profiles of the conversion X_{CH4}, the M module M_{module} (Eq. (17)) and the temperature T in the center. Moreover, maps of the 3D inlet region ($z \leq 0.1$ m) of the corresponding fields are also included in the figures. They consist of a two-dimensional slice of the fluid field along z together with a clip of the pellet region slightly above the fluid slice. In the sliced view of the conversion in the fluid field, the mass fraction ω_{CH4} is shown for the pellet fields. Fig. 9a shows the cup-mix temperature profiles along the bed. The average bed efficiency η_{bed} is 0.55 and radial temperature gradients are present throughout the reactor; the temperature difference ΔT between the center of the bed and the wall is 132 K. Thus, under the chosen operating conditions, the system is mass and heat transport limited. The conversion steadily increases to a value of $X_{CH4} = 22.50\,\%$, while the M_{module} reaches a value of 2.79 at the outlet of the reactor.

In contrast to the lab reactor model discussed in the last section, it is not possible to obtain a solution with full evaluation of the micro-kinetic scheme due to the large computational cost required. As a work-around and to evaluate the relative deviation of the predicted catalytic source terms against the corresponding reference $\epsilon_{\dot{s}}$, 50,000 randomly selected gas compositions within the pellet domain were extracted from the solution. From this subset of conditions, the catalytic source terms $\dot{s}_i$ were evaluated with the full micro-kinetic mechanism and an initial guess for the surface coverages (see supplementary information section S2.1). Fig. 10.a shows a parity plot, to compare the micro-kinetic solutions against the GRNN predictions. The GRNN performs well on the conditions that occur in the reactor simulation. However, in this subset, $\epsilon_{\dot{s}}$ is 1.82 %, higher than in any of the simulations with the lab reactor presented in the last section (see Table 4). This is due to deviations resulting from irrelevant conditions ($\dot{s}_i < 1{\cdot}10^{-8}\,\mathrm{kmol{\cdot}m^{-2}s^{-1}}$), mainly in $\dot{s}_{\mathrm{CO}}$ and $\dot{s}_{\mathrm{CO2}}$. Those conditions are likely under-represented in the training dataset (see Section 2.4). As discussed in the last section, full uniform sampling across all variables or an adaptive dataset design could potentially improve accuracy. Nevertheless, the small rates have a negligible influence on the overall conversion observed in the reactor. Neglecting them ($\dot{s}_i < 1{\cdot}10^{-8}\,\mathrm{kmol\,m^{-2}\,s^{-1}}$), results in a $\epsilon_{\dot{s}}$ of 0.71 %.

Similarly to the accuracy, the speed-up was not evaluated like in the last section. Instead, the speed-up was determined for individual selected timesteps. In the first step, the industrial reactor was run until convergence, saving all fields at different iteration steps ($\{0, 100, 500, 1000, 2000\}$). In the second step, the saved fields were used as initial conditions for simulations with full evaluation of the micro-kinetic scheme and with employed GRNN. Each simulation ran for eleven steps. The average of the last ten steps were used for the evaluation of the *total speed-up* (Eq. (18)) and the *chemistry speed-up* (Eq. (19)). The first iteration was neglected, as it may show initialization overheads that may alter the comparison. The results are reported in Fig. 9.b.

The bar chart shows a similar trend to the speed-up evaluated for the lab reactor (see Fig. 7). At the beginning of the simulation, both the *chemistry speed-up* and the *total speed-up* are at their maximum. In the first set of iterations the *chemistry speed-up* averages 88.0 and the *total speed-up* averages 39.5. From there, both values decrease rapidly and then remain on roughly the same plateau for the rest of the simulation, averaging 45.0 and 21.1, respectively. The lower observed speed-up in the beginning of the simulation compared to the last section can be accounted to neglecting the initial iteration, which is the most demanding.

With the employed GRNN, the solver required about 20 h on 32 CPUs to obtain a converged solution, with close to no loss of information. Reducing the number of CPUs is of course an option. Assuming linear scaling of computational time with CPUs, a converged result could be obtained in about three days on a computer with eight CPUs. The proposed methodology, thus, makes simulations of this scale feasible for a broader range of users.

3.4. Case study: Is the lab reactor a representative model for an industrial scale reactor?

It is widely acknowledged that the coupling of transport with kinetics in the actual geometry of interest is pivotal for the comprehension and optimization of heterogenous processes. Moreover, particle-resolved CFD can provide valuable insights [5,36]. The deployment of NNs for catalytic rate prediction has notably reduced the computational burden. This approach permits the simulation of considerably larger and more complex reactor geometries with minimal loss of accuracy. It is now feasible to conduct simulations at scales that were previously deemed impractical, including industrially relevant packed-bed reactors. This development allows for a more comprehensive representation of reactor behavior, encompassing finer details and more extensive spatial domains. Furthermore, an increase in model size facilitates the development of hierarchical models, whereby insights gained from detailed, high-resolution simulations can be used to inform and improve lower-fidelity models for faster, system-wide analysis [73–75]. This multiscale approach can facilitate to more effective optimization, design, and scale-up of catalytic reactors, ultimately accelerating the development of new catalytic processes and technologies.

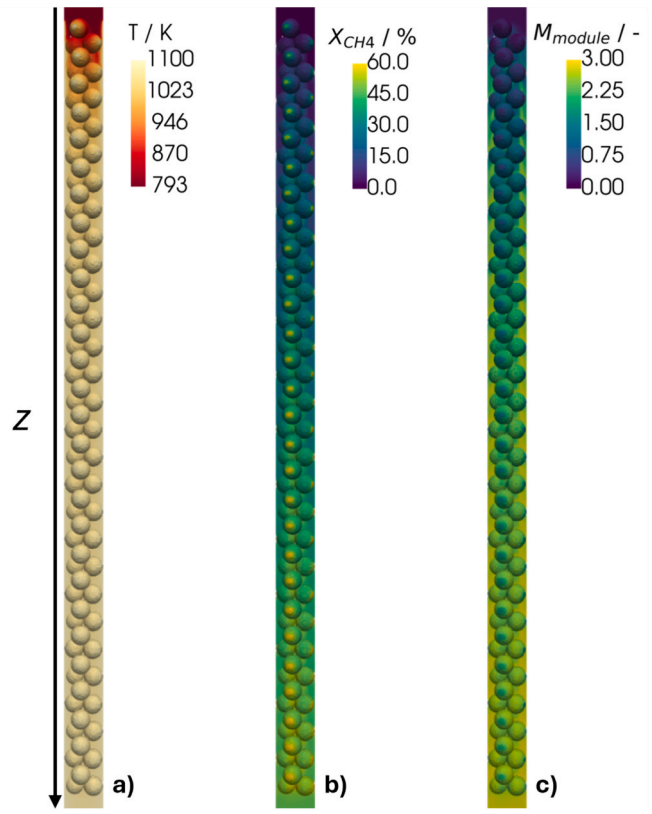

Fig. 11. Fields of the converged solution of the lab reactor with employed GRNN surrogate under the conditions listed in Table 3 and $U_{\mathrm{in}} = 0.0762\,\mathrm{m\,s^{-1}}$: In a) the T-field, in b) the X_{CH4}-field and the M_{module}-field in c).

The previous section introduces the industrial reactor model but focuses on the assessment of the employed GRNN. Here, the differences in the behavior of both reactor models are discussed to highlight the benefits of the proposed methodology and the larger feasible scales that can now be simulated. In contrast to the presented results of the previous sections, the external heating of the reactor tubes is adjusted so that only the section from the beginning of the packed bed is heated. The two reactors are operated under the conditions listed in Table 3. However, due to the different particle-to-tube-diameters, the catalyst loadings differ between both reactors. In the lab reactor and in the industrial reactor, pellets occupy approximately 47 % and 62 % of the volume of the empty tube, respectively. In order to account for the different catalyst loadings, both reactors are operated at the same mass based space-velocity *GHSV*, $7.74\,\mathrm{m^3_{gas}\,kg^{-1}_{cat}\,hr^{-1}}$; the industrial reactor with inlet velocity $U_{\mathrm{in}} = 0.1\,\mathrm{m\,s^{-1}}$ and the lab reactor with $U_{\mathrm{in}} = 0.0762\,\mathrm{m\,s^{-1}}$.

Fig. 11 and Fig. 12 illustrate the temperature field T in a), the conversion of methane field X_{CH4} in b) and the M module field M_{module} (Eq. (17)) in c) of the converged simulation of the lab reactor and of the industrial, respectively. The fluid domain is represented as an axial slice, and the pellets are visualized in three dimensions. In Fig. 12, after 20 cm, the packed bed is intersected by a 90°-cylinder cut-out, allowing a view of the bed interior. Additionally, a zoomed-in view of a single clipped pellet is provided to highlight the local effect of the coupling between transport and chemistry.

As expected, due to the different tube diameters, the cup-mix tem-

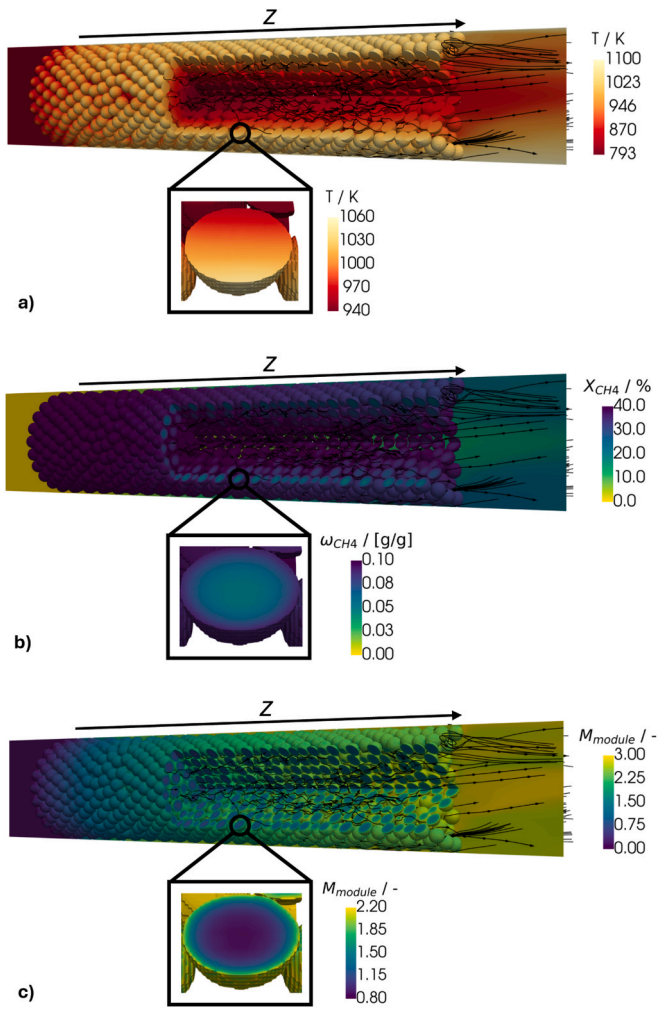

Fig. 12. Fields of the converged solution of the industrial reactor under the conditions listed in Table 3 and $U_{in} = 0.1\,m\,s^{-1}$: In a) the T-field, in b) the X_{CH4}-field for the fluid domain and the mass fraction ω_{CH4} for the pellet domain and the M_{module}-field in c).

perature in the lab reactor rises more quickly. In the lab reactor the temperature quickly reaches a constant value, close to the external one, (Fig. 11.a). In contrast, in the industrial reactor, the temperature (Fig. 12.a) was found to increase steadily but did not reach T_{wall} (see Table 3). At the end of the bed and in the axial center, the temperature remains at 966 K. The impact of the temperature is evident in the X_{CH4}-field (Fig. 11.b/Fig. 12.b) in both reactors, as the steam-reforming reaction rate (R1) increases with rising temperature. This increases the mass transfer limitation in the lab reactor, which is reflected in the average bed efficiency η_{bed} [59] of 0.51 and 0.56 in the lab reactor and in the industrial reactor, respectively.

For a quantitative comparison, in Fig. 13a. the cup-mix T and in Fig. 13b. the cup-mix of X_{CH4} for the fluid domain and the mass fraction ω_{CH4} for the pellet domain and M_{module} of both reactors is plotted against the axial position z. Although both reactors have been operated under the same conditions and the same *GHSV*, as discussed above, heat and mass transport differ due to the different particle-to-tube-diameters. When considering only X_{CH4}, the industrial reactor converts 21.9 % of methane, which is 48.1 % less than observed in the lab reactor with $X_{CH4} = 45.5\,\%$. On the one hand, the lab reactor heats up more quickly (see Fig. 13.a). Consequently, the average reaction rates are higher in the lab reactor.

On the other hand, the flow fields differ due to distinct bed packings. Consequently, the residence time distributions are likely to differ substantially between the reactors. Furthermore, due to the quicker rise in temperature, the fluid velocity increases more quickly in the lab reactor, which distorts the assumption of equal *GHSVs*. In this particular example, the discrepancy in temperature fields is presumably the predominant factor contributing to the increased conversion in the lab reactor. Nevertheless, it is evident that flow fields exert an influence on the coupling between transport and chemical kinetics and thus, it is crucial to investigate the actual geometry of interest.

4. Conclusion

In this study, we implemented a Global Reaction Neural Network (GRNN) surrogate model into the catalyticFOAM solver, thereby enabling the acceleration of catalytic rate evaluations within CFD simulations. The GRNN surrogate was trained to predict reaction rates for methane steam reforming under a wide range of operating conditions. In comparison to simulations with full evaluation of the micro-kinetic scheme, our findings show that a single GRNN model, employed on multiple reactor simulations, consistently achieves highly accurate results with average deviations of less than 0.5 % and 1 % in the species mole fractions and in the predicted catalytic source terms, respectively. Furthermore, the implementation of the GRNN model resulted in a 63-fold speed-up in the chemistry sub-step and a 19-fold total simulation speed-up for the lab-scale reactor. We further demonstrated the applicability of this approach to an industrial scale packed-bed reactor, which, to our knowledge, represents the largest fixed-bed reactor simulation case with micro-kinetic level of detail published to this day. With the GRNN acceleration, an industrial scale CFD simulation converged within 22 h using only 32 cores. This marks a substantial improvement over previous computational efforts in catalytic CFD.

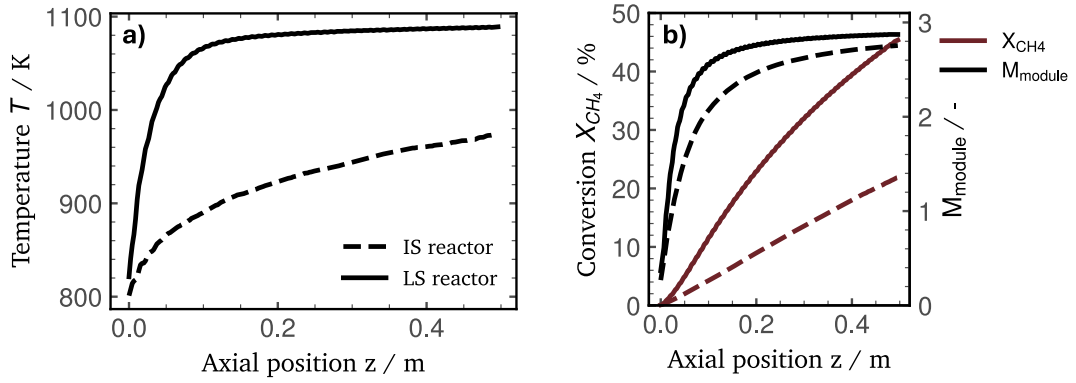

Fig. 13. Cup-mix profiles of the lab reactor (solid line) and the industrial reactor (dashed lines). In a) the cup-mix of T and in b) the cup-mixes of M_{module} (Eq. (17)) and X_{CH4}. The lab reactor and the industrial reactor were run with the conditions listed in Table 3 and $U_{in} = 0.0762\,m\,s^{-1}$ and $U_{in} = 0.1\,m\,s^{-1}$ respectively.

Moreover, the approach facilitates the development of hierarchical models.

In this work, we have successfully pushed the boundaries for particle-resolved CFD simulations, making them a viable option for larger, industrially relevant geometries. The incorporation of machine learning-driven surrogate models, such as GRNNs, into CFD frameworks significantly reduces the computational cost while preserving detailed chemical information. Consequently, simulations that were previously inaccessible due to high computational cost are now feasible, enabling more efficient and detailed studies of reactor design and optimization in heterogeneous catalysis.

CRediT authorship contribution statement

Felix Biermann: Writing – original draft, Methodology, Investigation, Data curation, Conceptualization. **Riccardo Uglietti:** Writing – review & editing, Supervision, Methodology, Conceptualization. **Felix A. Döppel:** Writing – review & editing, Methodology. **Tim Kircher:** Writing – review & editing, Methodology, Investigation. **Mauro Bracconi:** Writing – review & editing. **Matteo Maestri:** Writing – review & editing, Software. **Martin Votsmeier:** Writing – review & editing, Supervision, Software, Methodology, Funding acquisition, Conceptualization.

Declaration of competing interest

The authors declare that they have no known competing financial interests or personal relationships that could have appeared to influence the work reported in this paper.

Acknowledgements

The authors want to thank the German Federal Ministry of Economic Affairs and Climate Action (BMWK) for funding this research and ThyssenKrupp Uhde GmbH, Umicore AG & Co. KG and Umesoft GmbH for their technical, financial and advisory support in the framework of the “SuNiPro” project (FKZ 03EN2120A-C). The authors gratefully acknowledge the computing time provided on the high-performance computer Lichtenberg at the NHR Centers NHR4CES at TU Darmstadt. This is funded by the Federal Ministry of Education and Research, and the state governments participating *on the basis of the resolutions of the GWK for national high performance computing at universities.*

Appendix A. Supplementary data

Supplementary data to this article can be found online at https://doi.org/10.1016/j.cej.2025.163598.

Data availability

Data will be made available on request.

References

[1] G.D. Wehinger, M. Ambrosetti, R. Cheula, Z.-B. Ding, M. Isoz, B. Kreitz, K. Kuhlmann, M. Kutscherauer, K. Niyogi, J. Poissonnier, R. Réocreux, D. Rudolf, J. Wagner, R. Zimmermann, M. Bracconi, H. Freund, U. Krewer, M. Maestri, Quo vadis multiscale modeling in reaction engineering? – A perspective, Chem. Eng. Res. Des. 184 (2022) 39–58, https://doi.org/10.1016/j.cherd.2022.05.030.

[2] H. Freund, K. Sundmacher, Towards a methodology for the systematic analysis and design of efficient chemical processes, Chem. Eng. Process. - Process Intesif. 47 (2008) 2051–2060, https://doi.org/10.1016/j.cep.2008.07.011.

[3] H. Freund, J. Maußner, M. Kaiser, M. Xie, Process intensification by model-based design of tailor-made reactors, Curr. Opin. Chem. Eng. 26 (2019) 46–57, https://doi.org/10.1016/j.coche.2019.08.003.

[4] M.P. Dudukovic, Frontiers in reactor engineering, Science 325 (2009) 698–701, https://doi.org/10.1126/science.1174274.

[5] A. Bruix, J.T. Margraf, M. Andersen, K. Reuter, First-principles-based multiscale modelling of heterogeneous catalysis, Nat. Catal. 2 (2019) 659–670, https://doi.org/10.1038/s41929-019-0298-3.

[6] D.W. Agar, M. Bertau, M. Börnhorst, M. Busch, M. Casapu, P. Claus, K. Herrera Delgado, D. Demtröder, O. Deutschmann, R. Dittmeyer, DECHEMA Gesellschaft für Chemische Technik und Biotechnologie e.V. (September) (2023).

[7] M. Bracconi, M. Maestri, Training set design for machine learning techniques applied to the approximation of computationally intensive first-principles kinetic models, Chem. Eng. J. 400 (2020) 125469, https://doi.org/10.1016/j.cej.2020.125469.

[8] M. Bracconi, M. Maestri, A. Cuoci, In situ adaptive tabulation for the CFD simulation of heterogeneous reactors based on operator-splitting algorithm, AIChE J 63 (2017) 95–104, https://doi.org/10.1002/aic.15441.

[9] S. Matera, M. Maestri, A. Cuoci, K. Reuter, Predictive-quality surface reaction chemistry in real reactor models: integrating first-principles kinetic monte carlo simulations into computational fluid dynamics, ACS Catal. 4 (2014) 4081–4092, https://doi.org/10.1021/cs501154e.

[10] R. Uglietti, M. Bracconi, M. Maestri, Development and assessment of speed-up algorithms for the reactive CFD–DEM simulation of fluidized bed reactors, React. Chem. Eng. 5 (2020) 278–288, https://doi.org/10.1039/C9RE00440H.

[11] S.B. Pope, Computationally efficient implementation of combustion chemistry using in situ adaptive tabulation, Combust. Theor. Model. 1 (1997) 41–63, https://doi.org/10.1080/713665229.

[12] E.A. Daymo, M. Hettel, O. Deutschmann, G.D. Wehinger, Accelerating particle-resolved CFD simulations of catalytic fixed-bed reactors with DUO, Chem. Eng. Sci. 250 (2022) 117408, https://doi.org/10.1016/j.ces.2021.117408.

[13] G.M. Goldin, Z. Ren, S. Zahirovic, A cell agglomeration algorithm for accelerating detailed chemistry in CFD, Combust. Theor. Model. 13 (2009) 721–739, https://doi.org/10.1080/13647830903154542.

[14] M. Maestri, D. Livio, A. Beretta, G. Groppi, Hierarchical refinement of microkinetic models: assessment of the role of the WGS and r-WGS pathways in CH 4 partial oxidation on Rh, Ind. Eng. Chem. Res. 53 (2014) 10914–10928, https://doi.org/10.1021/ie501570b.

[15] M. Rein, The partial-equilibrium approximation in reacting flows, Phys. Fluids A 4 (1992) 873–886, https://doi.org/10.1063/1.858267.

[16] S.H. Lam, Using CSP to understand complex chemical kinetics, Combust. Sci. Technol. 89 (1993) 375–404, https://doi.org/10.1080/00102209308924120.

[17] U. Maas, S.B. Pope, Implementation of simplified chemical kinetics based on intrinsic low-dimensional manifolds, Symp. (Int.) Combust. 24 (1992) 103–112, https://doi.org/10.1016/S0082-0784(06)80017-2.

[18] U. Maas, S.B. Pope, Simplifying chemical kinetics: intrinsic low-dimensional manifolds in composition space, Combust. Flame 88 (1992) 239–264, https://doi.org/10.1016/0010-2180(92)90034-M.

[19] S.H. Lam, D.A. Goussis, The CSP method for simplifying kinetics, Int. J. Chem. Kinet. 26 (1994) 461–486, https://doi.org/10.1002/kin.550260408.

[20] M. Maestri, D. Vlachos, A. Beretta, G. Groppi, E. Tronconi, Steam and dry reforming of methane on Rh: microkinetic analysis and hierarchy of kinetic models, J. Catal. 259 (2008) 211–222, https://doi.org/10.1016/j.jcat.2008.08.008.

[21] R. Li, A.A. Konnov, G. He, F. Qin, D. Zhang, Chemical mechanism development and reduction for combustion of NH3/H2/CH4 mixtures, Fuel 257 (2019) 116059, https://doi.org/10.1016/j.fuel.2019.116059.

[22] K.E. Niemeyer, C.-J. Sung, Mechanism reduction for multicomponent surrogates: a case study using toluene reference fuels, Combust. Flame 161 (2014) 2752–2764, https://doi.org/10.1016/j.combustflame.2014.05.001.

[23] K.E. Niemeyer, C.-J. Sung, M.P. Raju, Skeletal mechanism generation for surrogate fuels using directed relation graph with error propagation and sensitivity analysis, Combust. Flame 157 (2010) 1760–1770, https://doi.org/10.1016/j.combustflame.2009.12.022.

[24] M. Kutscherauer, Particle-resolved CFD simulation of catalytic fixed bed reactors for maleic anhydride production, 2024.

[25] M. Kutscherauer, S.D. Anderson, S. Böcklein, G. Mestl, T. Turek, G.D. Wehinger, A conjugated heat and mass transfer model to implement reaction in particle-resolved CFD simulations of catalytic fixed bed reactors, Eng. Appl. Comput. Fluid Mech. 18 (2024) 2292100, https://doi.org/10.1080/19942060.2023.2292100.

[26] M. Kutscherauer, G.D. Wehinger, Particle-resolved CFD simulation of diluted catalytic fixed bed reactors for formaldehyde production, ACS Eng. Au (2025), https://doi.org/10.1021/acsengineeringau.5c00012.

[27] B. Partopour, A.G. Dixon, Resolved-particle fixed bed CFD with microkinetics for ethylene oxidation, AIChE J. 63 (2017) 87–94, https://doi.org/10.1002/aic.15422.

[28] M. Votsmeier, Efficient implementation of detailed surface chemistry into reactor models using mapped rate data, Chem. Eng. Sci. 64 (2009) 1384–1389, https://doi.org/10.1016/j.ces.2008.12.006.

[29] O. Deutschmann, Computational fluid dynamics simulation of catalytic reactors: part 6. makrokinetics and transport processes, handbook of heterogeneous, Catalysis (2008) 1811–1828, https://doi.org/10.1002/9783527610044.hetcat0097.

[30] M. Klingenberger, O. Hirsch, M. Votsmeier, Efficient interpolation of precomputed kinetic data employing reduced multivariate Hermite Splines, Comput. Chem. Eng. 98 (2017) 21–30, https://doi.org/10.1016/j.compchemeng.2016.12.005.

[31] M. Votsmeier, A. Scheuer, A. Drochner, H. Vogel, J. Gieshoff, Simulation of automotive NH3 oxidation catalysts based on pre-computed rate data from mechanistic surface kinetics, Catal. Today 151 (2010) 271–277, https://doi.org/10.1016/j.cattod.2010.01.018.

[32] B. Partopour, A.G. Dixon, Computationally efficient incorporation of microkinetics into resolved-particle CFD simulations of fixed-bed reactors, Comput. Chem. Eng. 88 (2016) 126–134, https://doi.org/10.1016/j.compchemeng.2016.02.015.
[33] T. Nien, J.P. Mmbaga, R.E. Hayes, M. Votsmeier, Hierarchical multi-scale model reduction in the simulation of catalytic converters, Chem. Eng. Sci. 93 (2013) 362–375, https://doi.org/10.1016/j.ces.2013.01.059.
[34] A. Scheuer, O. Hirsch, R. Hayes, H. Vogel, M. Votsmeier, Efficient simulation of an ammonia oxidation reactor using a solution mapping approach, Catal. Today 175 (2011) 141–146, https://doi.org/10.1016/j.cattod.2011.03.036.
[35] S. Matera, W.F. Schneider, A. Heyden, A. Savara, Progress in accurate chemical kinetic modeling, simulations, and parameter estimation for heterogeneous catalysis, ACS Catal. 9 (2019) 6624–6647, https://doi.org/10.1021/acscatal.9b01234.
[36] M. Bracconi, Intensification of catalytic reactors: a synergic effort of multiscale modeling machine learning and additive manufacturing, Chem. Eng. Process.-Process Intensification 181 (2022) 109148, https://doi.org/10.1016/j.cep.2022.109148.
[37] F.A. Döppel, M. Votsmeier, Efficient machine learning based surrogate models for surface kinetics by approximating the rates of the rate-determining steps, Chem. Eng. Sci. 262 (2022) 117964, https://doi.org/10.1016/j.ces.2022.117964.
[38] F. Döppel, T. Wenzel, R. Herkert, B. Haasdonk, M. Votsmeier, Goal-oriented two-layered kernel models as automated surrogates for surface kinetics in reactor simulations, Chem. Ing. Tech. (2024) cite.202300178, https://doi.org/10.1002/cite.202300178.
[39] B. Partopour, R.C. Paffenroth, A.G. Dixon, Random Forests for mapping and analysis of microkinetics models, Comput. Chem. Eng. 115 (2018) 286–294, https://doi.org/10.1016/j.compchemeng.2018.04.019.
[40] K. Reuter, M. Scheffler, First-principles kinetic Monte Carlo simulations for heterogeneous catalysis: application to the CO oxidation at RuO2(110), Phys. Rev. B 73 (2006) 45433, https://doi.org/10.1103/PhysRevB.73.045433.
[41] T. Hülser, B. Kreitz, C.F. Goldsmith, S. Matera, Multilevel on-the-fly sparse grids for coupling coarse-grained and high fidelity models in heterogeneous catalysis, Comput. Chem. Eng. 194 (2025) 108922, https://doi.org/10.1016/j.compchemeng.2024.108922.
[42] F.A. Döppel, M. Votsmeier, Efficient neural network models of chemical kinetics using a latent asinh rate transformation, React. Chem. Eng. 8 (2023) 2620–2631, https://doi.org/10.1039/D3RE00212H.
[43] B. Klumpers, T. Luijten, S. Gerritse, E. Hensen, I. Filot, Direct coupling of microkinetic and reactor models using neural networks, Chem. Eng. J. 475 (2023) 145538, https://doi.org/10.1016/j.cej.2023.145538.
[44] S. Kasiraju, D.G. Vlachos, LearnCK: mass conserving neural network reduction of chemistry and species of microkinetic models, React. Chem. Eng. 9 (2023) 119–131, https://doi.org/10.1039/D3RE00279A.
[45] A. Fedorov, A. Perechodjuk, D. Linke, Kinetics-constrained neural ordinary differential equations: artificial neural network models tailored for small data to boost kinetic model development, Chem. Eng. J. 477 (2023) 146869, https://doi.org/10.1016/j.cej.2023.146869.
[46] T. Kircher, F.A. Döppel, M. Votsmeier, Global reaction neural networks with embedded stoichiometry and thermodynamics for learning kinetics from reactor data, Chem. Eng. J. 485 (2024) 149863, https://doi.org/10.1016/j.cej.2024.149863.
[47] F.A. Döppel, M. Votsmeier, Robust mechanism discovery with atom conserving chemical reaction neural networks, Proc. Combust. Inst. 40 (2024) 105507, https://doi.org/10.1016/j.proci.2024.105507.
[48] P.O. Sturm, S.J. Silva, 2024. A nudge to the truth: atom conservation as a hard constraint in models of atmospheric composition using a species-weighted correction. ACS EST Air, acsestair.4c00220. Doi:10.1021/acsestair.4c00220.
[49] P.O. Sturm, A.S. Wexler, Conservation laws in a neural network architecture: enforcing the atom balance of a Julia-based photochemical model (v0.2.0), Geosci. Model Dev. 15 (2022) 3417–3431, https://doi.org/10.5194/gmd-15-3417-2022.
[50] F. Sorourifar, Y. Peng, I. Castillo, L. Bui, J. Venegas, J.A. Paulson, Physics-enhanced neural ordinary differential equations: application to industrial chemical reaction systems, Ind. Eng. Chem. Res. 62 (2023) 15563–15577, https://doi.org/10.1021/acs.iecr.3c01471.
[51] T. Kircher, M. Votsmeier, Machine learning surrogate models for mechanistic kinetics: embedding atom balance and positivity, J. Phys. Chem. Lett. 16 (2025) 4715–4723, https://doi.org/10.1021/acs.jpclett.5c00602.
[52] A. Fedorov, D. Linke, Extrapolation problems in kinetic modelling of catalytic reactions with neural networks, in: Proceedings of the 24th Conference Information Technologies - Applications and Theory (ITAT 2024), Drienica, Slovakia, September 20-24, 2024, CEUR-WS.org, 2024, pp. 24–30.
[53] T. Kircher, F.A. Döppel, M. Votsmeier, Embedding physics into neural ODEs to learn kinetics from integral reactors, Computer Aided Chemical Engineering 53 (2024) 817–822, https://doi.org/10.1016/B978-0-443-28824-1.50137-X.
[54] T. Kircher, M. Votsmeier, Learning kinetics from non-ideal reactors by implicitly solved finite volumes and global reaction neural networks (Preprint), ChemRxiv (2024), https://doi.org/10.26434/chemrxiv-2024-pgqr6.
[55] M. Maestri, A. Cuoci, Coupling CFD with detailed microkinetic modeling in heterogeneous catalysis, Chem. Eng. Sci. 96 (2013) 106–117, https://doi.org/10.1016/j.ces.2013.03.048.
[56] E. Shustorovich, The UBI-QEP method: a practical theoretical approach to understanding chemistry on transition metal surfaces, Surf. Sci. Rep. 31 (1998) 1–119, https://doi.org/10.1016/S0167-5729(97)00016-2.
[57] D. Micale, C. Ferroni, R. Uglietti, M. Bracconi, M. Maestri, Computational fluid dynamics of reacting flows at surfaces: methodologies and applications, Chem. Ing. Tech. 94 (2022) 634–651, https://doi.org/10.1002/cite.202100196.
[58] OpenFOAM (v8.0), OpenFOAM Foundation, https://openfoam.org/.
[59] T. Maffei, G. Gentile, S. Rebughini, M. Bracconi, F. Manelli, S. Lipp, A. Cuoci, M. Maestri, A multiregion operator-splitting CFD approach for coupling microkinetic modeling with internal porous transport in heterogeneous catalytic reactors, Chem. Eng. J. 283 (2016) 1392–1404, https://doi.org/10.1016/j.cej.2015.08.080.
[60] A. Burcat, B. Ruscic, Chemistry, Third millenium ideal gas and condensed phase thermochemical database for combustion (with update from active thermochemical tables), 2005.
[61] ONNX Runtime developers, ONNX Runtime (v1.19), Microsoft Corporation, https://onnxruntime.ai/, 2018.
[62] J.A. Dumesic, Analyses of reaction schemes using de donder relations, J. Catal. 185 (1999) 496–505, https://doi.org/10.1006/jcat.1999.2523.
[63] A. Cuoci, A. Frassoldati, T. Faravelli, E. Ranzi, OpenSMOKE++: an object-oriented framework for the numerical modeling of reactive systems with detailed kinetic mechanisms, Comput. Phys. Commun. 192 (2015) 237–264, https://doi.org/10.1016/j.cpc.2015.02.014.
[64] X. Glorot, Y. Bengio, Understanding the difficulty of training deep feedforward neural networks, in: Proceedings of the Thirteenth International Conference on Artificial Intelligence and Statistics, PMLR, Chia Laguna Resort, Sardinia, Italy, 2010, pp. 249–256.
[65] B. Partopour, A.G. Dixon, An integrated workflow for resolved-particle packed bed models with complex particle shapes, Powder Technol. 322 (2017) 258–272, https://doi.org/10.1016/j.powtec.2017.09.009.
[66] P.M. Plehiers, G.F. Froment, Coupled simulation of heat transfer and reaction in a steam reforming furnace, Chem. Eng. Technol. 12 (1989) 20–26, https://doi.org/10.1002/ceat.270120105.
[67] ESI-OpenCFD, OpenFoam-ESI (v2206), https://www.openfoam.com/.
[68] D. Micale, M. Bracconi, M. Maestri, Increasing computational efficiency of CFD simulations of reactive flows at catalyst surfaces through dynamic load balancing, ACS Eng. Au 4 (2024) 312–324, https://doi.org/10.1021/acsengineeringau.3c00066.
[69] A. Géron, Hands-on machine learning with Scikit-Learn, Keras, and TensorFlow: Concepts, tools, and techniques to build intelligent systems, third ed., O'Reilly, Beijing, Boston, Farnham, Sebastopol, Tokyo, 2023.
[70] A. Sanchez-Gonzalez, J. Godwin, T. Pfaff, R. Ying, J. Leskovec, P. Battaglia, Learning to Simulate Complex Physics with Graph Networks, in: Proceedings of the 37th International Conference on Machine Learning, 2020, pp. 8459–8468.
[71] Z. Li, N. Kovachki, C. Choy, B. Li, J. Kossaifi, S. Otta, M.A. Nabian, M. Stadler, C. Hundt, K. Azizzadenesheli, A. Anandkumar, Geometry-Informed Neural Operator for Large-Scale 3D PDEs, in: Advances in Neural Information Processing Systems, Curran Associates, Inc, 2023, pp. 35836–35854.
[72] A. Marcato, J.E. Santos, G. Boccardo, H. Viswanathan, D. Marchisio, M. Prodanović, Prediction of local concentration fields in porous media with chemical reaction using a multi scale convolutional neural network, Chem. Eng. J. 455 (2023) 140367, https://doi.org/10.1016/j.cej.2022.140367.
[73] S. Rebughini, M. Bracconi, A.G. Dixon, M. Maestri, A hierarchical approach to chemical reactor engineering: an application to micro packed bed reactors, React. Chem. Eng. 3 (2018) 25–33, https://doi.org/10.1039/C7RE00195A.
[74] M. Maestri, Escaping the trap of complication and complexity in multiscale microkinetic modelling of heterogeneous catalytic processes, Chem. Commun. (Camb) 53 (2017) 10244–10254, https://doi.org/10.1039/C7CC05740G.
[75] A.B. Mhadeshwar, D.G. Vlachos, Hierarchical multiscale mechanism development for methane partial oxidation and reforming and for thermal decomposition of oxygenates on Rh, J. Phys. Chem. B 109 (2005) 16819–16835, https://doi.org/10.1021/jp052479t.